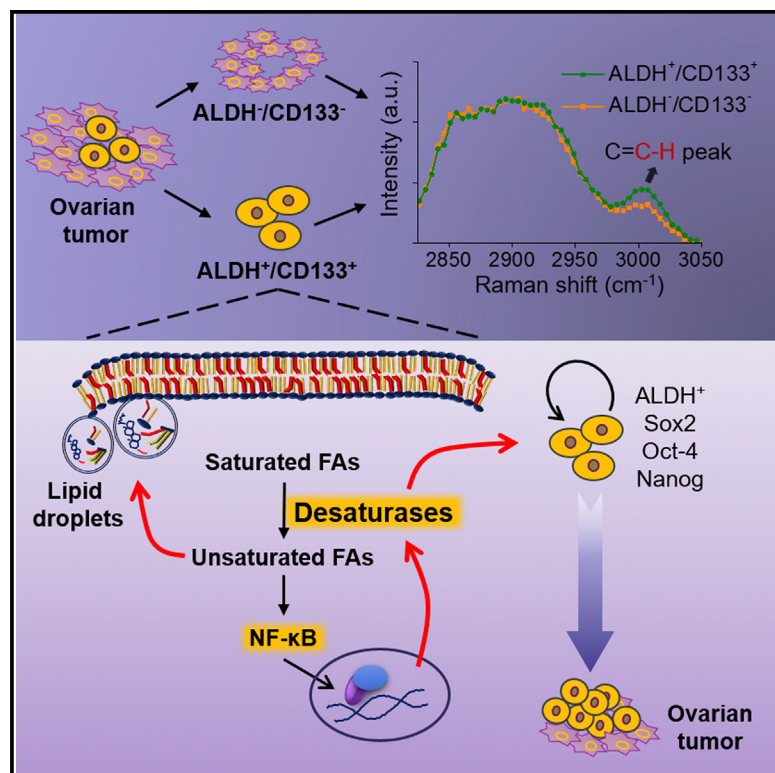


# Lipid Desaturation Is a Metabolic Marker and Therapeutic Target of Ovarian Cancer Stem Cells

## Graphical Abstract



## Authors

Junjie Li, Salvatore Condello,  
Jessica Thomes-Pepin, ...,  
Thomas D. Hurley, Daniela Matei,  
Ji-Xin Cheng

## Correspondence

daniela.matei@northwestern.edu (D.M.),  
jcheng@purdue.edu (J.-X.C.)

## In Brief

Cheng and colleagues using Raman spectroscopic imaging find that ovarian cancer stem cells contain unusually high levels of unsaturated lipids and show evidence that this metabolic difference could be used as a marker for these cells and as a new target for CSC-specific therapy.

## Highlights

- Ovarian cancer stem cells have high levels of unsaturated lipids
- Blocking lipid desaturation impairs cancer stemness and tumor initiation capacity
- The NF-κB pathway directly regulates the expression of lipid desaturases
- Lipid desaturase inhibitors inactivate the NF-κB pathway

# Lipid Desaturation Is a Metabolic Marker and Therapeutic Target of Ovarian Cancer Stem Cells

Junjie Li,<sup>1,10</sup> Salvatore Condello,<sup>2,10</sup> Jessica Thomes-Pepin,<sup>3</sup> Xiaoxiao Ma,<sup>4</sup> Yu Xia,<sup>4</sup> Thomas D. Hurley,<sup>5,6</sup> Daniela Matei,<sup>2,7,8,\*</sup> and Ji-Xin Cheng<sup>1,4,9,11,\*</sup>

<sup>1</sup>Weldon School of Biomedical Engineering, Purdue University, West Lafayette, IN 47907, USA

<sup>2</sup>Department of Obstetrics and Gynecology, Feinberg School of Medicine, Northwestern University, Chicago, IL 60611, USA

<sup>3</sup>Department of Obstetrics and Gynecology, Indiana University, Indianapolis, IN 46202, USA

<sup>4</sup>Department of Chemistry, Purdue University, West Lafayette, IN 47907, USA

<sup>5</sup>Department of Biochemistry and Molecular Biology, Indiana University School of Medicine, Indianapolis, IN 46202, USA

<sup>6</sup>Indiana University Simon Cancer Center, Indiana University School of Medicine, Indianapolis, IN 46202, USA

<sup>7</sup>Jesse Brown VA Medical Center, Chicago, IL 60612, USA

<sup>8</sup>Robert H. Lurie Comprehensive Cancer Center, Chicago, IL 60611, USA

<sup>9</sup>Purdue University Center for Cancer Research, Purdue University, West Lafayette, IN 47907, USA

<sup>10</sup>Co-first author

<sup>11</sup>Lead Contact

\*Correspondence: daniela.matei@northwestern.edu (D.M.), jcheng@purdue.edu (J.-X.C.)

<http://dx.doi.org/10.1016/j.stem.2016.11.004>

## SUMMARY

Lack of sensitive single-cell analysis tools has limited the characterization of metabolic activity in cancer stem cells. By hyperspectral-stimulated Raman scattering imaging of single living cells and mass spectrometry analysis of extracted lipids, we report here significantly increased levels of unsaturated lipids in ovarian cancer stem cells (CSCs) as compared to non-CSCs. Higher lipid unsaturation levels were also detected in CSC-enriched spheroids compared to monolayer cultures of ovarian cancer cell lines or primary cells. Inhibition of lipid desaturases effectively eliminated CSCs, suppressed sphere formation *in vitro*, and blocked tumor initiation capacity *in vivo*. Mechanistically, we demonstrate that nuclear factor  $\kappa$ B (NF- $\kappa$ B) directly regulates the expression levels of lipid desaturases, and inhibition of desaturases blocks NF- $\kappa$ B signaling. Collectively, our findings reveal that increased lipid unsaturation is a metabolic marker for ovarian CSCs and a target for CSC-specific therapy.

## INTRODUCTION

Cancer stem cells (CSCs), also recognized as tumor-initiating cells, represent a small population of cancer cells that have the ability to self-renew and initiate tumors *in vivo* (Bjerkvig et al., 2005). CSCs are resistant to conventional therapies and are responsible for tumor relapse after chemotherapy (Jordan et al., 2006; Pattabiraman and Weinberg, 2014) and development of distant metastases (Jordan et al., 2006). Understanding their unique characteristics and vulnerabilities will enable the development of CSC-targeting therapies with the ultimate goal of overcoming tumor relapse and metastasis.

Recent studies have focused on blocking signaling pathways or genetic programs that fuel cellular “stemness.” For example, epithelial to mesenchymal transition (EMT) is emerging as a key program in CSCs required for initiation of metastasis (Visvader and Lindeman, 2008). Related signaling pathways, like Wnt and transforming growth factor  $\beta$  (TGF- $\beta$ ), are recognized as new targets for CSC-specific therapy (Pattabiraman and Weinberg, 2014). The Hedgehog and Notch pathways implicated in the self-renewal of CSCs (Zhou et al., 2009) are being targeted, and specific inhibitors have recently entered clinical development. In ovarian cancer, the Mullerian Inhibiting Substance was proposed as a potential targeting strategy for chemotherapy-resistant CSCs (Meirelles et al., 2012; Szotek et al., 2006). However, as the development of technologies enabling the study of rare populations has lagged, one underexplored niche remains understanding the CSC metabolism.

So far, only limited studies have begun to address this niche. A recent report suggested that glucose played an important role maintaining the side population in non-small lung and colon cancer models and that inhibition of glycolysis blocked this population (Liu et al., 2014). A few studies have linked lipogenesis to CSCs. Specifically, inhibition of fatty acid synthase was shown to suppress the growth of breast cancer stem-like cells *in vivo* (Pandey et al., 2011); the peroxisome proliferator-activated receptor  $\gamma$  (PPAR $\gamma$ ) pathway was found important in maintaining the CSC properties of ERBB2-positive breast cancer cells partly by upregulating the de novo lipogenic pathway (Wang et al., 2013), and increased numbers of lipid droplets were identified in colorectal CSCs compared to differentiated cancer cells (Tirinato et al., 2015). Collectively, these studies point to lipogenesis as a potentially altered metabolic process in CSCs, but the precise mechanism by which lipids regulate stemness remains unknown.

In this study, we identify and characterize lipid unsaturation in ovarian CSCs by chemical imaging of single living cells through recently developed hyperspectral-stimulated Raman scattering (SRS) microscopy (Cheng and Xie, 2015; Zhang et al., 2015). This single-cell imaging study and mass spectrometry analysis show a significantly increased level of lipid unsaturation in

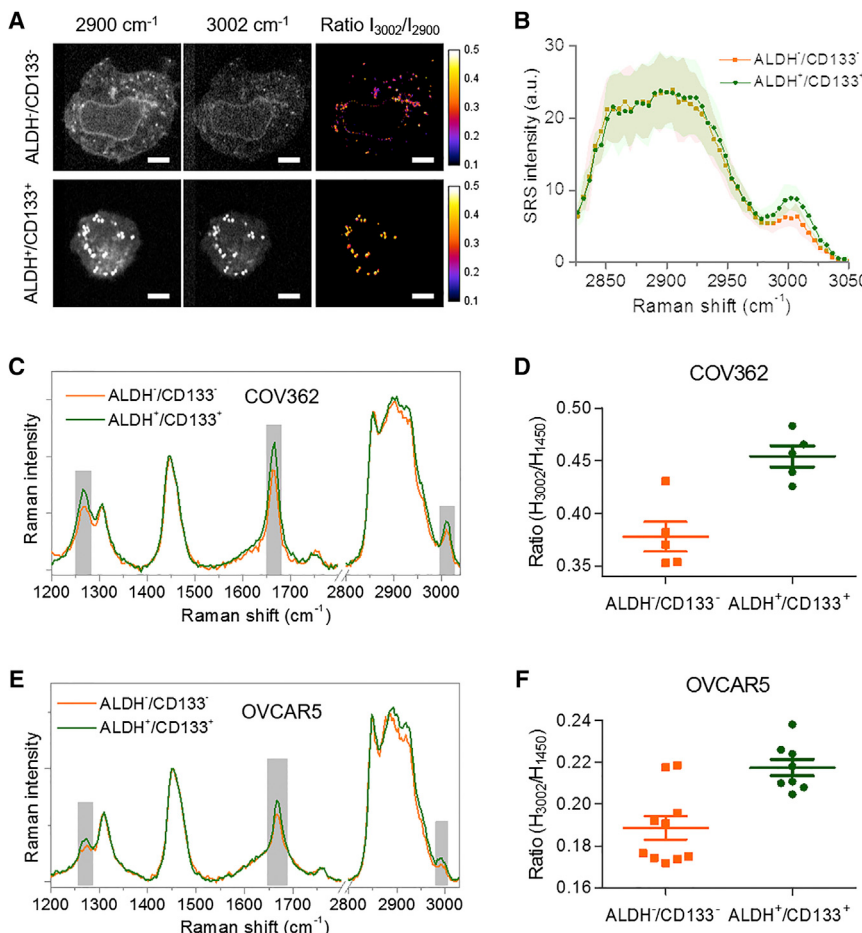


**Figure 1. Increased Lipid Unsaturation Level in Sorted ALDH<sup>+</sup>/CD133<sup>+</sup> Ovarian Cancer Cells**

(A) Representative hyperspectral SRS images of flow-sorted ALDH<sup>-</sup>/CD133<sup>-</sup> and ALDH<sup>+</sup>/CD133<sup>+</sup> COV362 cells. Images at 2,900 cm<sup>-1</sup>, 3,002 cm<sup>-1</sup>, and the intensity ratio image between 3,002 and 2,900 cm<sup>-1</sup> are shown. Scale bars, 10 μm.

(B) Average SRS spectra from the lipid droplets in ALDH<sup>-</sup>/CD133<sup>-</sup> (n = 3) and ALDH<sup>+</sup>/CD133<sup>+</sup> cells (n = 8). Shaded area indicates the standard deviation of SRS spectral measurements from different cells.

(C) Spontaneous Raman spectra taken from LDs in ALDH<sup>-</sup>/CD133<sup>-</sup> and ALDH<sup>+</sup>/CD133<sup>+</sup> sorted COV362 cells. The spectra were normalized by the height of the Raman peak at 1,450 cm<sup>-1</sup>. The differences at 1,264 cm<sup>-1</sup>, 1,660 cm<sup>-1</sup>, and 3,002 cm<sup>-1</sup> were highlighted in gray.

(D) Scatterplot of Raman spectra height ratio between the peaks at 3,002 cm<sup>-1</sup> and 1,450 cm<sup>-1</sup> in ALDH<sup>-</sup>/CD133<sup>-</sup> and ALDH<sup>+</sup>/CD133<sup>+</sup> COV362 cells. Each dot represents a single cell, and the bars indicate means ± SEM; p = 0.0005.

(E) Raman spectra taken from LDs in ALDH<sup>-</sup>/CD133<sup>-</sup> and ALDH<sup>+</sup>/CD133<sup>+</sup> OVCAR5 cells. The spectra were normalized by the height of peak at 1,450 cm<sup>-1</sup>. The differences at 1,264 cm<sup>-1</sup>, 1,660 cm<sup>-1</sup>, and 3,002 cm<sup>-1</sup> were highlighted in gray.

(F) Scatterplot of Raman spectra height ratio between the peaks at 3,002 cm<sup>-1</sup> and 1,450 cm<sup>-1</sup> in ALDH<sup>-</sup>/CD133<sup>-</sup> and ALDH<sup>+</sup>/CD133<sup>+</sup> OVCAR5 cells. Each dot represents a single cell, and the bars indicate means ± SEM; p = 0.0012.

See also Figure S1, Movie S1, and Movie S2.

flow-sorted ovarian CSCs (ALDH<sup>+</sup>/CD133<sup>+</sup>) compared to non-CSCs (ALDH<sup>-</sup>/CD133<sup>-</sup>) and in ovarian cancer (OC) cells growing as spheres compared to monolayers. Inhibition of lipid desaturases, either Δ9 (SCD1) or Δ6, impaired cancer cell stemness, suppressed sphere formation, and prevented tumor formation *in vivo*. We further identified the nuclear factor κB (NF-κB) pathway as a critical mechanism through which lipid desaturase inhibitors perturb the functions of CSCs. Collectively, our findings put forward lipid desaturation as a metabolic marker of ovarian CSCs and as a new target for CSC-specific therapy.

## RESULTS

### Increased Lipid Unsaturation in Isolated Ovarian CSCs Compared to Non-CSCs

We employed hyperspectral SRS microscopy to quantitatively analyze the composition of intracellular lipids inside single cells. ALDH<sup>+</sup>/CD133<sup>+</sup> cells, which have been previously described as cells possessing CSC characteristics (Flesken-Nikitin et al., 2014; Foster et al., 2013), were isolated from COV362, an ovarian cancer (OC) cell line. By tuning the Raman shift frame by frame, 50 images of individual ALDH<sup>-</sup>/CD133<sup>-</sup> and ALDH<sup>+</sup>/CD133<sup>+</sup> COV362 cells were recorded at the C-H vibration region from 2,800 to 3,050 cm<sup>-1</sup> with a step size of ~5 cm<sup>-1</sup> (Movie S1 and Movie S2). Inside each cell, the C-H bond rich lipid droplets

were highlighted in the context of relatively weaker signals from protein and nucleotides. Initial analysis of the images at 2,850 cm<sup>-1</sup>, where the CH<sub>2</sub> symmetric stretch vibration resides, revealed an increase of total amount of lipid droplets in ALDH<sup>+</sup>/CD133<sup>+</sup> cells. An in-depth comparison revealed that lipid droplets in ALDH<sup>+</sup>/CD133<sup>+</sup> cells had a stronger signal at 3,002 cm<sup>-1</sup> than those in ALDH<sup>-</sup>/CD133<sup>-</sup> cells (Figure 1A). As the peak at 3,002 cm<sup>-1</sup> is known to be from the vibration of =C-H bonds mostly in unsaturated lipids (Movasagh et al., 2007), our data suggests that ALDH<sup>+</sup>/CD133<sup>+</sup> CSC cells have a higher level of unsaturated lipids. To eliminate the influence of the total number of C-H bonds, we used the peak around 2,900 cm<sup>-1</sup>, contributed by C-H stretch vibrations in all the lipids (Movasagh et al., 2007), to normalize the SRS intensity at 3,002 cm<sup>-1</sup>. After normalization, the ratio of SRS intensity at 3,002 cm<sup>-1</sup> to that at 2,900 cm<sup>-1</sup> ( $I_{3,002}/I_{2,900}$ ) was found to be significantly higher in ALDH<sup>+</sup>/CD133<sup>+</sup> cells than that in ALDH<sup>-</sup>/CD133<sup>-</sup> cells (Figure 1A). The difference of the peak intensity at 3,002 cm<sup>-1</sup> became more obvious when we plotted together the SRS spectra from different lipid droplets (Figure 1B). Quantitatively, we found a statistically significant difference between the two groups in terms of lipid unsaturation level (Figure S1A).

To confirm the above observation, we acquired full Raman spectra from individual LDs in both C-H stretch and fingerprint vibration regions. After normalization by the CH<sub>2</sub> bending vibration

peak at  $1,450\text{ cm}^{-1}$ , the Raman spectra clearly showed that the peak at  $1,264\text{ cm}^{-1}$  (in plane bending motion of  $=\text{C}-\text{H}$ ), the peak at  $1,660\text{ cm}^{-1}$  (stretching vibration of  $\text{C}=\text{C}$ ), and the peak at  $3,002\text{ cm}^{-1}$  (vibration of  $=\text{C}-\text{H}$ ) in  $\text{ALDH}^+/\text{CD133}^+$  cells were higher than those in  $\text{ALDH}^-/\text{CD133}^-$  cells (Figure 1C). In consistency with the hyperspectral SRS imaging data, the height ratios of the peak at  $3,002\text{ cm}^{-1}$  to the peak at  $1,450\text{ cm}^{-1}$  (Figure 1D),  $1,660\text{ cm}^{-1}$  to  $1,450\text{ cm}^{-1}$  (Figure S1B), and  $1,264\text{ cm}^{-1}$  to  $1,450\text{ cm}^{-1}$  (Figure S1C) all showed a significant increase of lipid unsaturation level in  $\text{ALDH}^+/\text{CD133}^+$  cells. To ensure that the findings are not cell line specific, we compared  $\text{ALDH}^+/\text{CD133}^+$  and  $\text{ALDH}^-/\text{CD133}^-$  populations isolated from OVCAR5 cells. After normalization by the  $1450\text{ cm}^{-1}$  peak, higher peak intensities at  $1,264\text{ cm}^{-1}$ ,  $1,660\text{ cm}^{-1}$ , and  $3,002\text{ cm}^{-1}$  were noted in  $\text{ALDH}^+/\text{CD133}^+$  OVCAR5 cells compared to  $\text{ALDH}^-/\text{CD133}^-$  OVCAR5 cells (Figure 1E). Quantitatively, the height ratio of the peak at  $3,002\text{ cm}^{-1}$  to the peak at  $1,450\text{ cm}^{-1}$  was significantly higher in CSCs compared to non-CSCs (Figure 1F). These results collectively demonstrate increased lipid unsaturation in ovarian CSCs compared to non-CSCs.

### Increased Lipid Unsaturation in Spheroids Compared to Monolayer Cultures

It is known that CSCs have the ability to proliferate as spheres when cultured under non-adherent conditions (Ponti et al., 2005; Zhou and Zhang, 2008). Thus, we utilized CSC-rich spheroids as a second model to validate our observations. Hyperspectral SRS imaging was conducted to analyze lipid composition of COV362 cells grown either as monolayers or as spheres under similar serum-free conditions (Movie S3 and Movie S4). Using the intensity ratio between  $3,002\text{ cm}^{-1}$  and  $2,900\text{ cm}^{-1}$ , we observed an increased unsaturation level in spheres compared to monolayer cultures (Figure 2A). As most cells in spheroids showed higher levels of unsaturation, it is possible that both CSCs and other progenitor cells present in spheres are rich in unsaturated lipids (Ponti et al., 2005). Comparison of SRS spectral profile (Figure 2B) and quantitative analysis of the intensity ratio ( $I_{3,002}/I_{2,900}$ ) (Figure S2A) further confirmed the difference in lipid unsaturation levels between monolayers and spheres. Based on the height ratio of the peak at  $3,002\text{ cm}^{-1}$  to the peak at  $1450\text{ cm}^{-1}$ , Raman spectral analysis of COV362, OVCAR5, and primary cells derived from malignant OC ascites (total 4 patients, Table S1) quantitatively demonstrates elevated lipid unsaturation levels in spheres compared to monolayers cells (Figure 2C).

Although the SRS imaging and Raman spectral analysis focused on lipid droplets, which are storage sites of neutral lipids mainly in the form of triglycerides and sterol esters, we speculated that the increased unsaturation in lipid droplets was part of an altered lipid metabolic network in CSCs. To test the hypothesis, we performed whole lipid analysis by mass spectrometry. First, we extracted free fatty acids from cells grown as monolayers or spheres (Ma and Xia, 2014) and analyzed by electrospray ionization mass spectrometry (ESI-MS). As shown in the mass spectra (Figure S2B), the major components of free fatty acids in both monolayer and sphere cultures derived from OVCAR5 cells were 18:1 (e.g., oleic acid) and 18:0 (e.g., stearic acid). When normalized by the peak intensity of 18:0, the peak intensity of 18:1 in spheres

was found to be significantly higher than that in cells grown as monolayers (Figure S2C). Consistent results were obtained in COV362 (Figure S2D) and primary OC cells isolated from malignant OC ascites (Figures S2E and S2F). Furthermore, using liquid chromatography-mass spectrometry (LC-MS), we performed a more quantitative and comprehensive analysis of fatty acids saponified from all lipids (Kamphorst et al., 2013). The levels of all measured saponified fatty acids, including palmitic (16:0), palmitoleic (16:1), stearic (18:0), oleic (18:1), linoleic (18:2), arachidonic (20:4), and docosahexaenoic acid (22:6), were significantly increased in cells grown as spheres compared to monolayer cultures (Figures 2D and S2G). These data are consistent with the proposed phenomenon of increased de novo lipogenesis in CSCs. Moreover, the ratio of unsaturated fatty acids (UFA) to saturated fatty acids (SFA) was significantly increased in COV362 (Figure 2E) and OVCAR5 (Figure S2H) cells grown as spheres, confirming the increased unsaturation level in lipid droplets measured by Raman spectral analysis. These results suggest that unsaturation level in lipid droplets can be used as a readout of intracellular activities of desaturases. Taken together, the increased lipid unsaturation in ovarian CSCs was validated through hyperspectral SRS imaging, Raman spectroscopy, and mass spectrometry, in different CSC models derived from cell lines and primary OC cells.

### The Increased Lipid Unsaturation Is Mediated by Lipid Desaturases

Intracellular lipids originate either from the uptake of extracellular lipids or through de novo synthesis. We have shown higher levels of lipid unsaturation in both flow-sorted  $\text{ALDH}^+/\text{CD133}^+$  cells grown in the presence of serum (Figures 1 and S1) and in spheroids grown in serum-free medium (Figures 2 and S2). To determine the source of increased unsaturated lipids in CSCs, we examined the contribution of de novo synthesis, which is mediated by three fatty acid desaturases  $\Delta 9$ ,  $\Delta 6$ , and  $\Delta 5$  (Santos and Schulze, 2012). Among the three desaturases,  $\Delta 9$  (stearoyl-CoA desaturase-1 [SCD1]) catalyzes the synthesis of monounsaturated fatty acids by adding one double bond to saturated fatty acids (mostly stearic acid), while the  $\Delta 6$  and  $\Delta 5$  desaturases are involved predominantly in the synthesis of polyunsaturated fatty acids (Nakamura and Nara, 2004). While lipid desaturases are expressed in the majority of ovarian tumors (data not shown) and other cancers (Roongta et al., 2011), they are enriched in CSCs. *SCD1* mRNA expression level was significantly higher in  $\text{ALDH}^+/\text{CD133}^+$  versus  $\text{ALDH}^-/\text{CD133}^-$  cells in both OVCAR5 (Figure 3A) and COV362 (Figure 3B) cell lines.

Small molecule inhibitors, CAY10566 that blocks SCD1 (Liu et al., 2007) and SC-26196 that blocks  $\Delta 6$  (Obukowicz et al., 1998), and small hairpin RNA (shRNA)-based downregulation were used to study further the function of desaturases in ovarian CSCs. Both inhibitors significantly reduced the lipid unsaturation levels in OC spheroids (Figures 3C and 3D). The SCD1 inhibitor was more potent than the  $\Delta 6$  inhibitor, perhaps because mono-unsaturated rather than polyunsaturated lipids contribute more significantly to the increased unsaturation levels in CSCs. To measure the effects of lipid desaturase inhibitors on metabolic flux from SFAs to UFAs, we deployed metabolic tracing with

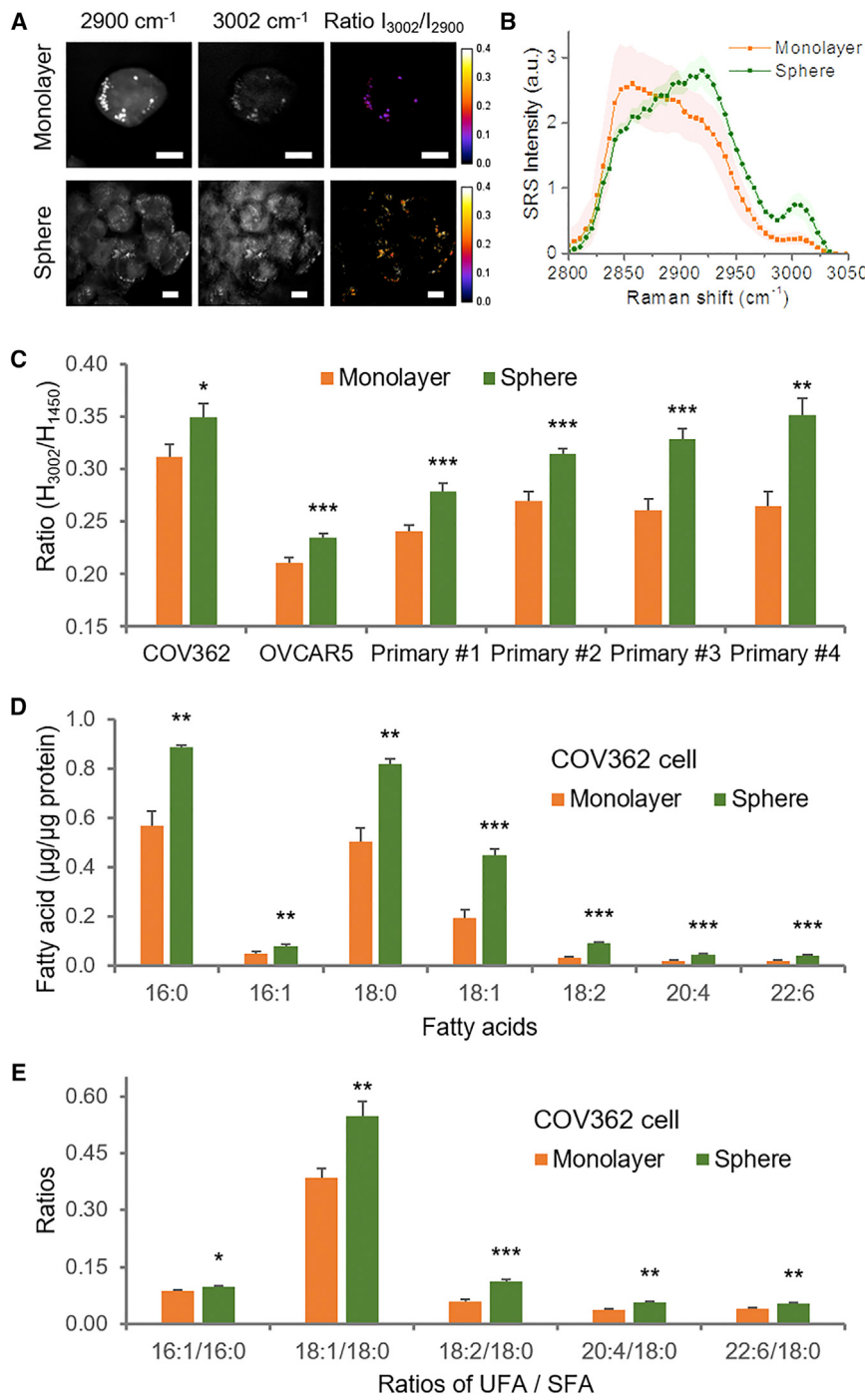


**Figure 2. Increased Lipid Unsaturation Level in Spheres Compared to Monolayer Cultures**

(A) Representative hyperspectral SRS images of COV362 cells grown as monolayers and spheres. Images at 2,900 cm<sup>-1</sup>, 3,002 cm<sup>-1</sup>, and the intensity ratio between 3,002 cm<sup>-1</sup> and 2,900 cm<sup>-1</sup> are shown. Scale bars, 10 µm.

(B) Average SRS spectra from the lipid droplets in COV362 monolayer (n = 6) and spheres (n = 6). Shaded area indicates the standard deviation of SRS spectral measurements from different cells.

(C) Quantitation of the height ratio between the =C-H peak at 3,002 cm<sup>-1</sup> and the C-H bending peak at 1,450 cm<sup>-1</sup> based on Raman spectral measurements in monolayers and spheres derived from COV362, OVCAR5, and primary cells isolated from malignant OC ascites of four patients. The data are shown as means + SEM; n ≥ 10.

(D) LC-MS measurement of fatty acids saponified from all lipids extracted from COV362 monolayer cultures and spheres. Fatty acids levels were normalized by total protein amount extracted from an equal number of cells.

(E) Quantitation of the ratios of unsaturated fatty acid (UFA) to saturated fatty acid (SFA) in COV362 monolayer and spheres. The data are shown as means + SD; n = 3. \*p < 0.05, \*\*p < 0.01, \*\*\*p < 0.001.

See also Figure S2, Table S1, Movie S3, and Movie S4.

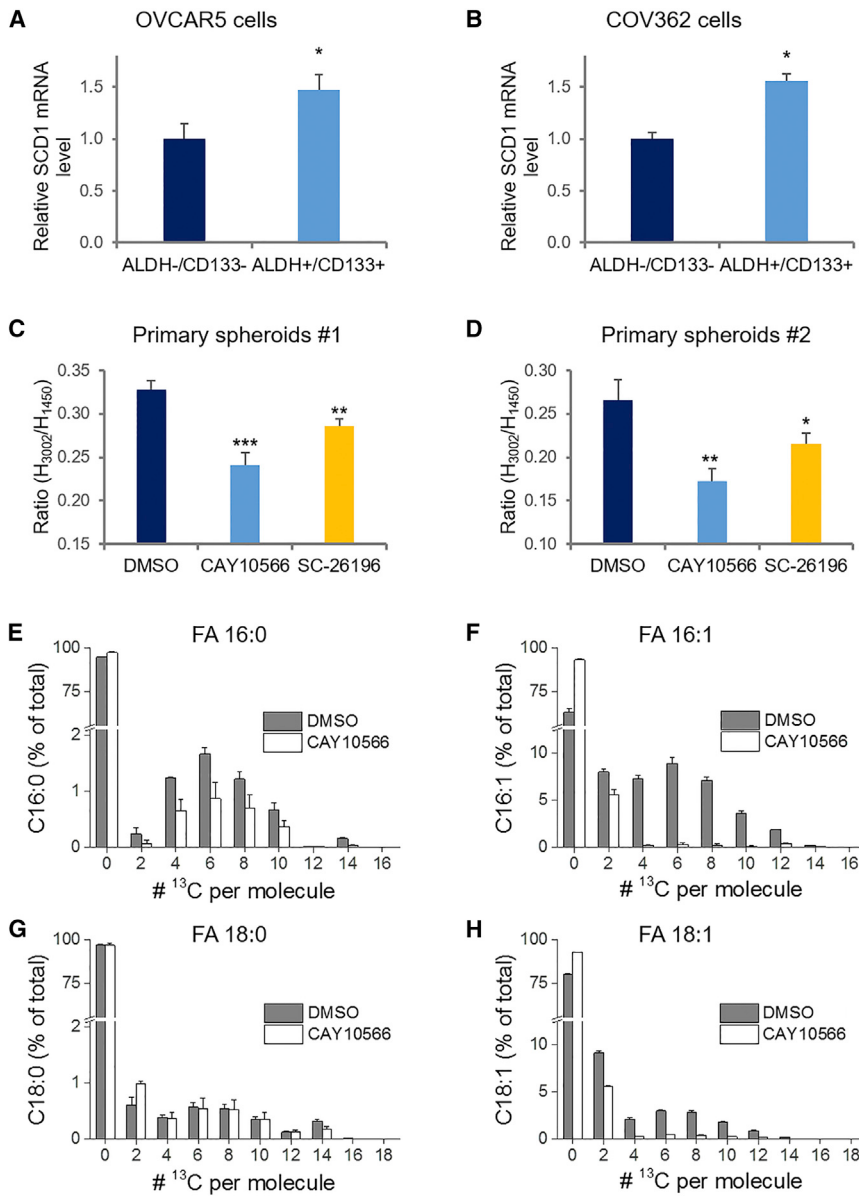
control transfected cells (Figures S3A–S3D). Collectively, these data support an essential role of lipid desaturases for the synthesis of UFAs in CSCs.

### Lipid Desaturases Contribute to the Maintenance of Cancer Cell Stemness

To test the functional significance of lipid desaturases relative to the known traits of CSCs, we measured the expression levels of CSC markers by qRT-PCR after desaturase inhibitor treatment or shRNA-based downregulation. Both CAY10566 and SC-26196 reduced ALDH1A1 mRNA expression levels in OVCAR5, COV362, and primary ovarian cancer spheroids (Figure 4A). Additionally, the expression levels of CSC-associated

transcription factors Sox2, Nanog, and Oct-4 were decreased by treatment with the inhibitors in OVCAR5, COV362, and primary spheroids (Figures 4B, S4A, and S4B). Similarly, knockdown of SCD1 by shRNA reduced the mRNA expression levels of ALDH1A1, Nanog, Sox2, and Oct-4, in both OVCAR5 (Figures 4C and S4C) and COV362 spheroids (Figures 4D and S4D). The reduction of stemness was further confirmed by a reduction in the ALDH<sup>+</sup> cell population after treatment with the inhibitors as measured by flow cytometry (Figure 4E). Overall, these

<sup>13</sup>C-labeled glucose and glutamine (Kamphorst et al., 2013). The relative abundances of <sup>13</sup>C-labeled fatty acids saponified from all lipids, including palmitic acid (16:0), palmitoleic acid (16:1), stearic acid (18:0), and oleic acid (18:1), were quantitatively analyzed by mass spectrometry. As shown in Figures 3E–3H, CAY10566 significantly suppressed the incorporation of <sup>13</sup>C into UFAs (FA 16:1 and FA 18:1), but not in SFAs (FA 16:0 and FA 18:0) in OVCAR5 spheroids. Similar effects were observed in cells in which SCD1 was knocked down by shRNA compared to shRNA



data support an important role of lipid desaturases in CSC maintenance.

### Inhibition of Lipid Desaturases Prevents Sphere Formation In Vitro and Tumorigenesis In Vivo

To determine the effect of desaturase inhibitors on the functions of CSCs, we examined the capacity of CSCs to form spheroids in vitro (Visvader and Lindeman, 2008) and initiate tumors in vivo. Both CAY10566 (Figure 5A) and SC-26196 (Figure 5B) effectively suppressed sphere formation in OVCAR5, COV362, and primary OC cells. The suppression of sphere proliferation was further confirmed by using the CCK-8 assay in OVCAR5, COV362, and primary OC cells (Figures S5A and S5B). Suppression of sphere formation was also observed in OVCAR5 (Figure S5C) and COV362 cells (Figure S5D), in which SCD1 was stably knocked down compared to shRNA

**Figure 3. Increased Desaturation in CSCs Is Due to Lipid Desaturases**

(A and B) qRT-PCR measurement of *SCD1* expression levels in ALDH<sup>-</sup>/CD133<sup>-</sup> and ALDH<sup>+</sup>/CD133<sup>+</sup> OVCAR5 (A) and COV362 (B) cells. The data are shown as means + SEM; n = 3.

(C and D) Raman spectral measurement of lipid unsaturation level in (C) primary spheres derived from patient #1 and (D) primary spheres derived from patient #2 treated with the SCD1 inhibitor CAY10566 or Δ6 inhibitor SC-26196 at 1.0  $\mu\text{M}$  for 6 days. The data are shown as means + SEM; n ≥ 10.

(E–H) LC-MS analysis of relative abundance of  $^{13}\text{C}$  incorporation into fatty acids 16:0 (E), 16:1 (F), 18:0 (G), and 18:1 (H) saponified from all lipids in OVCAR5 spheroids treated with DMSO or 1  $\mu\text{M}$  CAY10566 for 6 days. The data are shown as means + SD; n = 3. \*p < 0.05, \*\*p < 0.01, \*\*\*p < 0.001.

See also Figure S3.

control transfected cells. In contrast, OVCAR5 cells grown as monolayers (containing fewer CSCs) (Figure S5E) and normal human dermal fibroblasts (NHF544) (Figure S5F) were less sensitive to desaturase inhibitors compared to spheroids, supporting that lipid desaturation represents a CSC-specific target.

Next, to investigate the contribution of exogenous lipid uptake to ovarian CSCs proliferation, we measured sphere formation in the presence of several exogenous fatty acids (e.g., FA 16:0, 16:1, 18:0, 18:1, 18:2, 20:4, and 22:6). Fatty acids supplementation did not alter (positively or negatively) sphere proliferation and addition of exogenous lipids only partially rescued the inhibition exerted by desaturase inhibitors on sphere formation (Figures 5C and 5D, and S6A–S6E). These data suggest that CSCs rely on the de

novo fatty acid synthesis pathway, rather than on exogenous lipid uptake.

To measure the effects of desaturase inhibitors on tumor formation in vivo, we inoculated DMSO or inhibitor pretreated CSCs in the flanks of nude mice. Time-to-tumor formation and tumor volumes were measured. Pretreatment of ALDH<sup>+</sup>CD133<sup>+</sup> flow-sorted OVCAR5 cells with the desaturase inhibitors CAY10566 and SC-26196 significantly delayed the median time-to-tumor initiation from 14 days (DMSO) to 39 days and 23 days (Table S2), respectively. Pretreatment with CAY10566 (Figure 5E) or SC-20196 (Figure 5F) significantly suppressed tumor growth. Tumor weights (mean ± SEM) were significantly reduced from  $827 \pm 154$  mg (DMSO) to  $22 \pm 12$  mg by CAY10566 (Figure S6F) and from  $562 \pm 160$  mg (DMSO) to  $219 \pm 31$  mg by SC-26196 (Figure S6G). To verify the effects of the inhibitors on stemness, a tumor initiation assay was

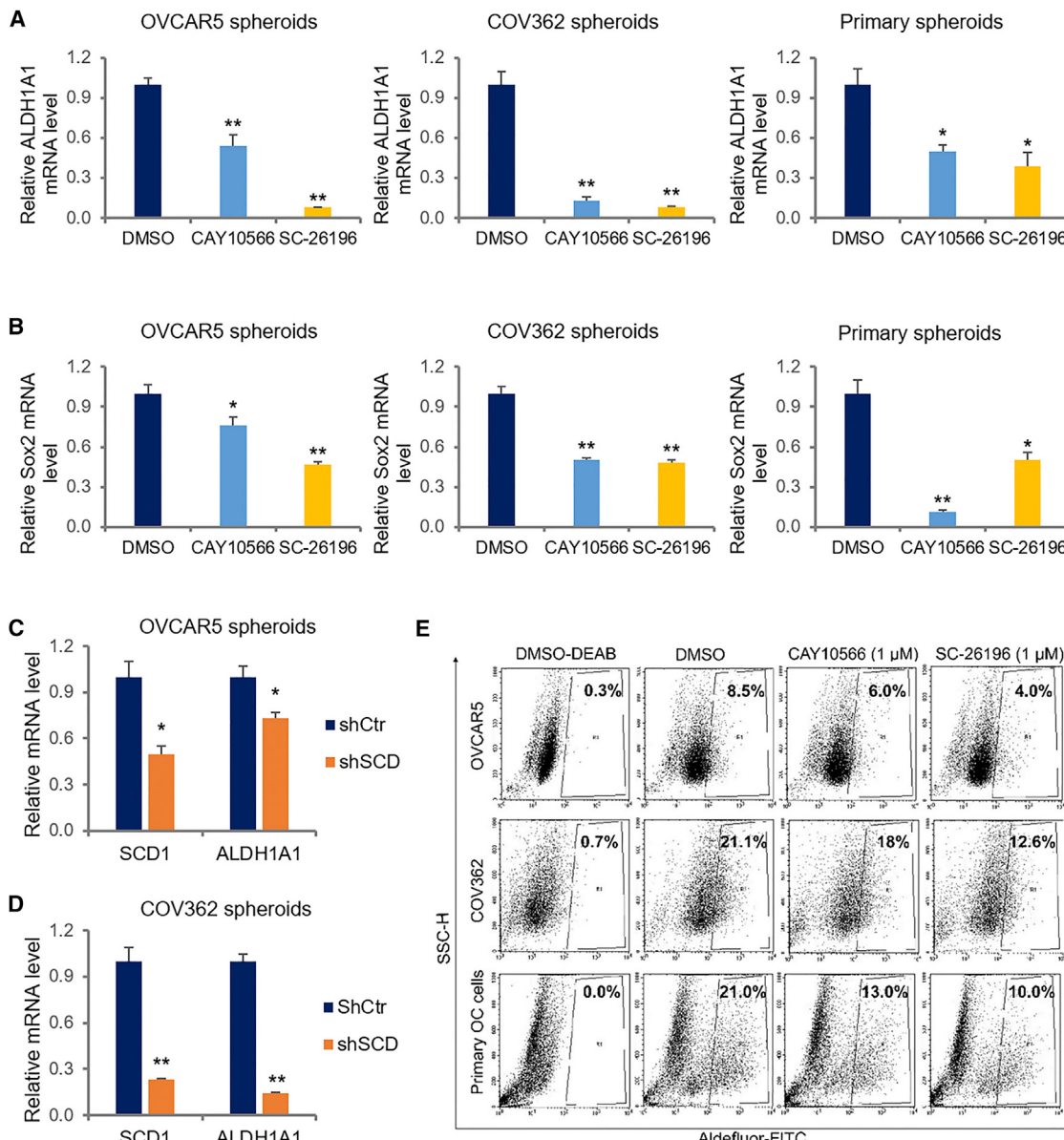


**Figure 4. Inhibition of Lipid Desaturation Impairs Ovarian Cancer Cell Stemness**

(A) RT-PCR measurement of *ALDH1A1* mRNA expression level in OVCAR5, COV362, and primary spheroids.

(B) RT-PCR measurement of *Sox2* mRNA expression level in OVCAR5, COV362, and primary spheroids. Treatment with CAY10566 or SC-26196 in spheroids was done at a concentration of 1.0  $\mu$ M for 6 days.

(C and D) RT-PCR measurement of *SCD1*, *ALDH1A1* mRNA expression level in OVCAR5 (C) and COV362 (D) cells stably transfected with scrambled control shRNA (shCtrl) or *SCD1* shRNA (shSCD). The data were shown as means + SEM; n = 3. \*p < 0.05, \*\*p < 0.01, \*\*\*p < 0.001.

(E) Flow cytometry analysis of *ALDH*<sup>+</sup> cells sorted from OVCAR5, COV362, and primary cells after CAY10566 or SC-26196 treatment at a concentration of 1.0  $\mu$ M for 6 days. DEAB was used as negative control.

See also Figure S4.

subsequently performed by using serial dilutions of CSCs flow sorted from OVCAR5 cell line. CAY10566 pretreatment reduced the frequency of tumor initiation to 20% (one out of five mice) when ~500 *ALDH*<sup>+</sup>/CD133<sup>+</sup> cells were used, 40% (two out of five mice) for ~1,000 CSCs, 80% (four out of five mice) for ~5,000 and ~10,000 CSCs, whereas tumors formed in all control groups (Figure 5G). Collectively, these data support that

blockade of lipid desaturation selectively suppresses the sphere formation and tumor initiation capacity of ovarian CSCs.

#### Inhibition of Lipid Desaturases Downregulates the NF- $\kappa$ B Pathway

Having shown the effects of desaturase inhibitors on sphere formation and tumorigenesis, we next explored the mechanism

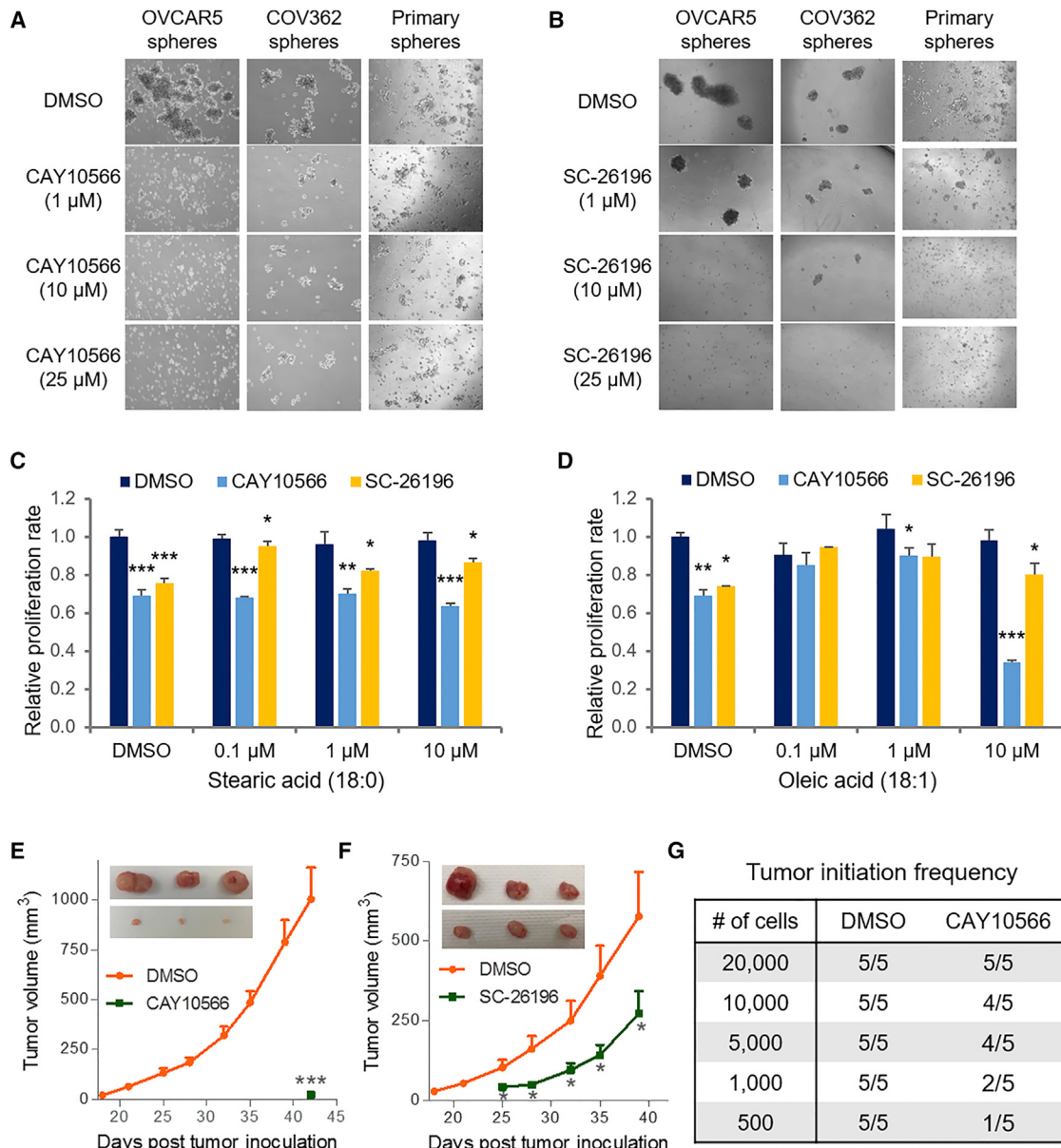


**Figure 5. Inhibition of Lipid Desaturation Prevents Sphere Growth In Vitro and Tumor Formation In Vivo**

(A and B) Representative images of OVCAR5, COV362 and primary spheres treated with CAY10566 (A) or SC-26196 (B) at indicated concentrations for 6 days. (C and D) Sphere proliferation of COV362 cells supplemented with fatty acid 18:0 (C) and 18:1 (D) at indicated concentrations and treated with CAY10566 or SC-26196 at 1  $\mu$ M for 6 days. Comparisons were performed between inhibitors-treated group and DMSO-treated group under the same concentrations of fatty acid supplementation ( $p$  value indicated by \*), or between DMSO groups under different concentrations of fatty acid supplementation ( $p$  value indicated by #). The data are normalized to the blank control (no fatty acid supplementation and treated with DMSO) and shown as means + SEM;  $n = 4$ .

(E and F) Growth curves of xenografts derived from DMSO ( $n = 7$ ) or CAY10566 ( $n = 6$ ) (E), and DMSO ( $n = 8$ ) or SC-26196 ( $n = 8$ ) (F) pretreated OVCAR5 cells grown in spheroids. The data are presented as means + SEM. Inset: tumor size comparison at the end of study (42 days after tumor cells inoculation). Upper: DMSO; lower: treated. \* $p < 0.05$ , \*\* $p < 0.01$ , \*\*\* $p < 0.001$ .

(G) Tumor initiation assay using serial dilution of OVCAR5 cells pretreated with DMSO or CAY10566 at 1  $\mu$ M. Cells were counted and then cultured for 6 days with the presence of DMSO or CAY10566 to allow sphere formation before injected into the mice. Five mice were used for each group.

See also Figures S5 and S6 and Table S2.

by which lipid desaturation alters the functions of CSCs. We first screened the effects of the inhibitors on various CSC-related signaling mechanisms by using pathway-specific qRT-PCR arrays. Both CAY10566 and SC-26196 downregulated

key stem cell-related signaling networks in OC spheroids, particularly the NF- $\kappa$ B, PI3K/Akt, Hedgehog, Notch, self-renewal, asymmetric division, migration, and metastasis pathways (Figures 6A and 6B). One of the most responsive

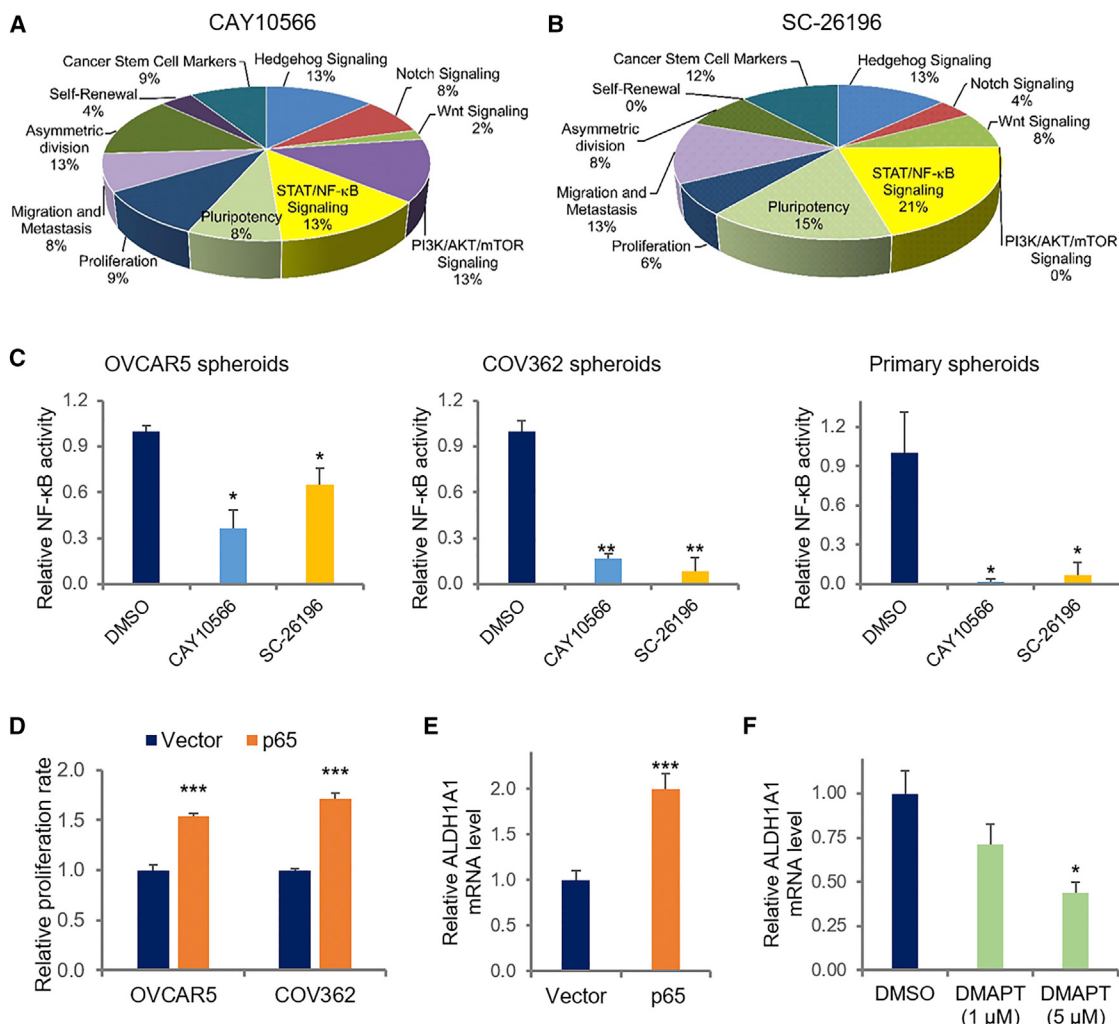


**Figure 6. Inhibition of Lipid Desaturation Downregulates the NF-κB Pathway**

(A and B) CSC genes preferentially downregulated by CAY10566 treatment compared to control (DMSO) (>2.0-fold) (A) or SC-26196 treatment compared to control (DMSO) (>2.0-fold) (B) were quantified by RT<sup>2</sup> Profiler PCR array in OVCAR5 spheroids treated with CAY10566 at 1 μM for 6 days. Pie chart analysis showing the downregulated genes (% of total) for each represented pathway in control versus treated spheres.

(C) NF-κB promoter activity measured by gene reporter assay in OVCAR5, COV362 and primary OC cells spheroids treated with CAY10566 or SC-26196 at 1 μM for 6 days.

(D) Proliferation of OVCAR5 and COV362 cells stably transduced with empty vector (pQCXIP) or with pQCXIP/p65 and grown as spheroids. The data are shown as means + SEM; n = 4.

(E) RT-PCR measurement of ALDH1A1 in COV362 spheroids stably transduced with empty vector (pQCXIP) or with pQCXIP/p65.

(F) RT-PCR measurement of ALDH1A1 mRNA levels in primary OC spheroids treated with NF-κB inhibitor, DMAPT, at indicated concentrations. The data are shown as means + SEM; n = 3. \*p < 0.05, \*\*p < 0.01, \*\*\*p < 0.001.

See also Figures S7A and S7B.

pathways to desaturase inhibition was NF-κB signaling, a key survival pathway in cancer, which has been also linked to cancer stemness (Shostak and Chariot, 2011). To confirm the suppression of NF-κB by desaturase inhibitors, we used an NF-κB reporter assay. Both CAY 10566 and SC-26196 significantly suppressed NF-κB transcriptional activity in OVCAR5, COV362, and primary OC spheres (Figure 6C). Confirming suppression of NF-κB activity, the mRNA expression levels of *IL-6* (Figure S7A) and *IL-8* (Figure S7B), known NF-κB target genes, were significantly downregulated by desaturase inhibitors in OC cells.

To investigate the link between NF-κB and the stem cell phenotype, p65 (relA), the active subunit of NF-κB, was overexpressed in ovarian cancer cells and the stem cell characteristics were evaluated. Indeed, overexpression of p65 increased ovarian cancer sphere proliferation in OVCAR5 and COV362 cells (Figure 6D). qRT-PCR demonstrated that the overexpression of p65 increased ALDH1A1 expression in COV362 cells (Figure 6E). Consistently, a small molecule inhibitor of NF-κB, dimethylaminoparthenolide (DMAPT) (Shanmugam et al., 2011), reduced ALDH1A1 expression in primary OC spheroids (Figure 6F). Together, these data support that NF-κB, as an

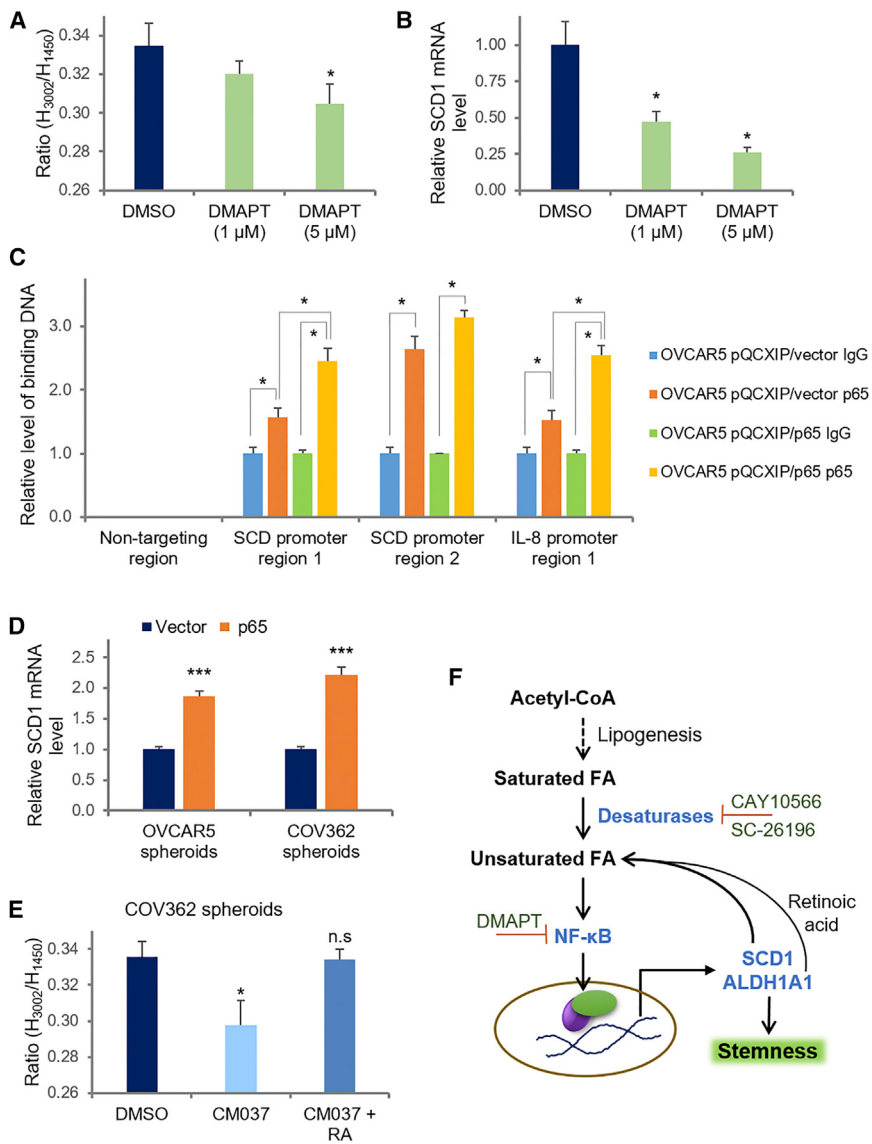


**Figure 7. NF-κB and ALDH1A1 Promote Lipid Unsaturation**

(A) Raman spectral measurement of lipid unsaturation level in OC spheroids treated with the NF-κB inhibitor, DMAPT, at indicated concentrations.  $n \geq 10$ .

(B) RT-PCR measurement of *SCD1* mRNA levels in primary OC spheroids treated with DMAPT at indicated concentrations.  $n = 3$ .

(C) ChIP demonstrates that p65 binds the *SCD1* promoter region. Immunoprecipitated chromatin with an antibody against p65 was used for qPCR amplification. Primers flanking two predicted p65-binding regions of the *SCD1* promoter (-215 to -206 and +79 to +88 bp) were used. Positive control was p65 antibody-immunoprecipitated chromatin amplified with primers for the IL8 promoter, a known p65 target. Negative controls were chromatin immunoprecipitated with IgG and amplified with *SCD1* promoter primers and chromatin immunoprecipitated with p65 antibody and amplified with primers to a region in the *SCD1* promoter located upstream of the predicted p65 binding sites.

(D) qRT-PCR measured *SCD1* mRNA expression levels in COV362 spheroids transfected with pQCXIP vector or pQCXIP/p65. The data are shown as means  $\pm$  SEM;  $n = 3$ .

(E) Raman spectral measurement of lipid unsaturation level in COV362 spheroids treated with ALDH1A1 inhibitor, CM037, or CM037 and retinoic acid for 6 days. The data are shown as means  $\pm$  SEM;  $n \geq 10$ . \* $p < 0.05$ , \*\* $p < 0.01$ , \*\*\* $p < 0.001$ , n.s., not significant.

(F) The proposed mechanism by which lipid desaturation is linked to cancer cell stemness. See also Figures S7C–S7H.

important pathway downregulated by desaturases inhibition, is involved in stem cell regulation.

#### NF-κB and ALDH Regulate Lipid Unsaturation

To further understand the mechanism by which NF-κB is linked to lipid desaturation and ovarian cancer cell stemness, ovarian cancer spheres were treated with the NF-κB inhibitor. DMAPT decreased both lipid unsaturation levels (Figure 7A) as well as *SCD1* mRNA expression levels in primary ovarian cancer spheres (Figure 7B). Next, to investigate whether NF-κB directly regulates the expression of desaturases, a promoter search motif identified two putative p65 (relA) binding sites at position -215 to -206 and at position +79 to +88 in the *SCD1* promoter (Figure S7C). The direct interaction between p65 and the *SCD1* promoter region was then confirmed by chromatin immunoprecipitation (ChIP) using a p65 antibody in OVCAR5 cells stably transduced with pQCXIP or pQCXIP/p65 (Figure 7C). Consistent with the proposed direct transcrip-

tional regulatory role of NF-κB, the overexpression of p65 significantly upregulated the expression levels of *SCD1* in OVCAR5 and COV362 spheroids (Figure 7D). IL8, a known p65 target gene was used as a positive control in these experiments (Figure S7D). Together, these results demonstrate that NF-κB directly regulates *SCD1* expression and promotes CSC characteristics.

We also detected increased lipid unsaturation in ALDH<sup>+</sup> (single marker) OC cells (Figure S7E). ALDH1A1 functions as a detoxification enzyme and is implicated in the conversion of retinol to retinoic acid (Ma and Allan, 2011; Marcato et al., 2011). ALDH1A1 is recognized as a stem cell marker in several tumor types, including ovarian cancer (Silva et al., 2011), but its involvement remains unclear. It has been proposed that its role in the maintenance of CSCs is related to regulation of cell differentiation mediated by retinoic acid signaling (Chute et al., 2006; Gineistier et al., 2009). To determine the potential mechanism by which ALDH1A1 may be involved in regulating lipid desaturation, we used a recently identified and highly specific ALDH1A1 inhibitor, CM037 (Condello et al., 2015). Treatment with CM037 potently decreased the mRNA expression levels of *SCD1* in primary OC spheres (Figure S7F), supporting a link between the two

pathways. Additionally, CM037 decreased lipid unsaturation levels in COV362 (Figure 7E), OVCAR5 (Figure S7G), and primary OC spheres (Figure S7H). Because ALDH1A1 regulates retinoic acid signaling (Ma and Allan, 2011), we next tested whether its effects on lipid unsaturation can be reversed by retinoic acid. The lipid unsaturation levels reduced by CM037 were successfully rescued by the addition of retinoic acid in COV362 (Figure 7E), OVCAR5 (Figure S7G), and primary OC spheres (Figure S7H). Taken together, these data suggest a role of ALDH1A1 in the regulation of lipid desaturation in ovarian CSCs mediated through retinoic acid signaling.

As summarized in Figure 7F, our studies revealed a functional role of altered lipid metabolism in ovarian CSCs. Through de novo lipogenesis and subsequent lipid desaturation, the unsaturated fatty acids promote activation of NF- $\kappa$ B, a key pathway involved in maintaining the CSC phenotype. In turn, the NF- $\kappa$ B pathway modulates the expression levels of lipid desaturases at the transcriptional level. Together, our data support a positive feedback loop between lipid metabolism and NF- $\kappa$ B signaling in regulating OC cell stemness.

## DISCUSSION

Since the first use of CD34 and CD38 as surface markers of leukemia stem cells, efforts to search for bona fide markers of CSCs have intensified. The lack of reliable methods to identify and isolate CSCs has remained one of the biggest challenges facing CSC research (Clevers, 2011). Current methods to enrich or isolate CSCs include surface marker labeling for flow cytometry sorting, side population sorting, and sphere culture (Zhou and Zhang, 2008). Surface markers have been widely used as the standard method to isolate CSCs. Some intracellular markers, such as aldehyde dehydrogenase (ALDH) have also been used alone or in combination with other markers. However, many of the CSC markers selected based on empirical assays are not necessarily linked to clear functional roles (Clevers, 2011; Visvader and Lindeman, 2008). Recently, Miranda-Lorenzo et al. (2014) reported that a strong intracellular autofluorescence signal, originating from riboflavin accumulation, can be used as a biomarker for epithelial CSCs. However, the precise function of the accumulated fluorophore remains unknown and the level of the autofluorescence signal can be easily altered by environmental changes, limiting its use as a reliable marker for CSCs.

Our study proposes a stable, universal, and functional metabolic marker for ovarian CSCs. By using Raman spectroscopic imaging, we identified an increase of lipid unsaturation levels in the lipid droplets of single ovarian CSCs derived from cell lines and human specimens. As the site for neutral lipid storage, LDs buffer the synthesis and consumption of lipids, which renders their composition relatively stable over time. Because unsaturated lipids are primarily derived from de novo synthesis, they are not easily subject to environmental changes. Indeed, we observed consistently increased lipid unsaturation in CSCs regardless of culture conditions (e.g., serum-enriched or serum-free media) in OC cell lines and human primary malignant cells. Raman spectral measurement is based on the ratio of unsaturated lipids to total lipids, instead of the absolute amount of unsaturated lipids, eliminating the change

induced by the total lipids amount. It is possible that increased unsaturated lipids are detectable in CSCs from other cancer types (unpublished data in pancreatic and leukemia cells), and future studies will address this concept more broadly. Combining this marker with Raman spectroscopic imaging could lead to a reliable and universal method for *in situ* detection of CSCs. Further refinement of Raman spectroscopic imaging-based techniques, such as coherent Raman scattering flow cytometry (Camp et al., 2009, 2011; Wang et al., 2008), would allow fast, noninvasive detection and isolation of CSCs.

As shown by single-cell spectroscopic imaging, CSCs are characterized by a higher conversion rate from saturated to unsaturated lipids, compared to differentiated cancer cells, a process mediated by fatty acid desaturases. We further observed that lipid desaturases are enriched in CSCs and can be targeted. By measuring key characteristics of stem cells *in vitro* and *in vivo*, including sphere formation and tumor initiation, we showed that lipid desaturases are critical to maintaining CSCs, suggesting that unlike most surface markers, unsaturated lipids possess definitive functions. Our data support further investigation of lipid desaturases as CSC-specific targets and development of combination strategies using these inhibitors with standard chemotherapy targeting the non-CSC population to improve disease control.

Finally, we identified a positive feedback loop involving the NF- $\kappa$ B pathway, ALDH1A1, and lipid desaturases in ovarian CSCs. A functional link between NF- $\kappa$ B as the master regulator of inflammation converging pathways and cancer has been established for other tumor models (Karin et al., 2002; Shostak and Chariot, 2011), and activation of NF- $\kappa$ B in stem cells has been recently reported (Jia et al., 2015). Here, we link NF- $\kappa$ B, lipid desaturases, and CSCs. Our data support that NF- $\kappa$ B regulates *SCD1* at the transcriptional level, that NF- $\kappa$ B activation promotes ovarian sphere proliferation, and in turn, desaturase inhibition blocks NF- $\kappa$ B activity and reduces cancer stemness. Interestingly, we show that IL-6, one of the known targets genes of NF- $\kappa$ B, is potently downregulated by the inhibitors. IL-6 has been recently linked to cancer stemness in multiple cancer models (Sansone et al., 2016; van der Zee et al., 2015). The exact mechanism by which NF- $\kappa$ B is inactivated by desaturase inhibitors in CSCs remains undefined. A possible explanation could be that the reduction of unsaturated lipids induced by the inhibitors directly blocks NF- $\kappa$ B given that unsaturated fatty acids, such as arachidonic acid (Camandola et al., 1996), oleic, and linoleic acid (Poletto et al., 2015), are known activators of the complex. Besides the NF- $\kappa$ B pathway, our PCR array assay showed that disruption of lipid desaturation also impaired other stem cell-associated pathways, which may contribute additionally to inhibiting CSCs. Unsaturated lipids are also known to modulate membrane fluidity (Nakamura and Nara, 2004), which could contribute to altered oncogenic signaling and impairment of stemness.

In all, our results discovered a new functional marker of ovarian CSCs, intimately linked to the NF- $\kappa$ B survival pathway and lipid metabolism. We propose that this marker represents a targetable metabolic vulnerability of recalcitrant stem cells, which should be exploited to improve the outcome of existing therapies.

## STAR★METHODS

Detailed methods are provided in the online version of this paper and include the following:

- KEY RESOURCES TABLE
- CONTACT FOR REAGENT AND RESOURCE SHARING
- EXPERIMENTAL MODEL AND SUBJECT DETAILS
  - Cell lines
  - Primary human cells
  - Subcutaneous xenograft mouse model
- METHOD DETAILS
  - Sphere formation assay
  - Aldefluor assay and Fluorescence-Activated Cell Sorting
  - Hyperspectral stimulated Raman scattering (SRS) imaging
  - Spontaneous Raman spectroscopy
  - Mass spectrometry analysis of fatty acids
  - Tumor initiation assays in subcutaneous xenograft mouse model
  - Generation of SCD1 stably knockdown cells
  - Stable retroviral transduction
  - Gene reporter assay
  - Reverse transcription-PCR (RT-PCR)
  - Chromatin immunoprecipitation (ChIP)
- QUANTIFICATION AND STATISTICAL ANALYSIS

## SUPPLEMENTAL INFORMATION

Supplemental Information includes seven figures, three tables, and four movies and can be found with this article online at <http://dx.doi.org/10.1016/j.stem.2016.11.004>.

## AUTHOR CONTRIBUTIONS

Conceptualization, J.-X.C. and D.M.; Methodology, J.L., S.C., D.M., and J.-X.C.; Investigation, J.L., S.C., and X.M.; Formal Analysis, J.L. and S.C.; Resources, J.T.-P., T.D., and Y.X.; Writing – Original Draft, J.L.; Writing – Review & Editing, all authors; Visualization, J.L., S.C., D.M., and J.-X.C.; Funding Acquisition, J.-X.C. and D.M..

## ACKNOWLEDGMENTS

The authors thank Leelyn Chong and Drs. Bin Liu, Chi Zhang, and Bakhtiyor Yakubov for technical support. The authors acknowledge the use of the metabolite profiling facility of the Bindley Bioscience Center at Purdue University. This work was supported by a VA Merit Award (BX000792-05A1), the NCI (CA198409 to D.M. and CA182608 to J.-X.C.), the Walther Cancer Foundation (to J.-X.C.), and the NIH (P30CA023168). J.L. and J.-X.C. are co-founders of Resarci Therapeutics LLC.

Received: January 4, 2016

Revised: August 10, 2016

Accepted: November 2, 2016

Published: December 29, 2016

## REFERENCES

- Bjerkvig, R., Tysnes, B.B., Aboody, K.S., Najbauer, J., and Terzis, A.J.A. (2005). Opinion: the origin of the cancer stem cell: current controversies and new insights. *Nat. Rev. Cancer* 5, 899–904.
- Camandola, S., Leonarduzzi, G., Musso, T., Varesio, L., Carini, R., Scavazza, A., Chiarpotto, E., Baeuerle, P.A., and Poli, G. (1996). Nuclear factor κB is activated by arachidonic acid but not by eicosapentaenoic acid. *Biochem. Biophys. Res. Commun.* 229, 643–647.
- Camp, C.H., Jr., Yegnanarayanan, S., Eftekhar, A.A., Sridhar, H., and Adibi, A. (2009). Multiplex coherent anti-Stokes Raman scattering (MCARS) for chemically sensitive, label-free flow cytometry. *Opt. Express* 17, 22879–22889.
- Camp, C.H., Jr., Yegnanarayanan, S., Eftekhar, A.A., and Adibi, A. (2011). Label-free flow cytometry using multiplex coherent anti-Stokes Raman scattering (MCARS) for the analysis of biological specimens. *Opt. Lett.* 36, 2309–2311.
- Cheng, J.-X., and Xie, X.S. (2015). Vibrational spectroscopic imaging of living systems: An emerging platform for biology and medicine. *Science* 350, aaa8870.
- Chua, H.L., Bhat-Nakshatri, P., Clare, S.E., Morimiy, A., Badve, S., and Nakshatri, H. (2007). NF-κB represses E-cadherin expression and enhances epithelial to mesenchymal transition of mammary epithelial cells: potential involvement of ZEB-1 and ZEB-2. *Oncogene* 26, 711–724.
- Chute, J.P., Muramoto, G.G., Whitesides, J., Colvin, M., Safi, R., Chao, N.J., and McDonnell, D.P. (2006). Inhibition of aldehyde dehydrogenase and retinoid signaling induces the expansion of human hematopoietic stem cells. *Proc. Natl. Acad. Sci. USA* 103, 11707–11712.
- Clevers, H. (2011). The cancer stem cell: premises, promises and challenges. *Nat. Med.* 17, 313–319.
- Condello, S., Morgan, C.A., Nagdas, S., Cao, L., Turek, J., Hurley, T.D., and Matei, D. (2015). β-Catenin-regulated ALDH1A1 is a target in ovarian cancer spheroids. *Oncogene* 34, 2297–2308.
- Flesken-Nikitin, A., Odai-Afotey, A.A., and Nikitin, A.Y. (2014). Role of the stem cell niche in the pathogenesis of epithelial ovarian cancers. *Mol. Cell. Oncol.* 1, e963435.
- Foster, R., Buckanovich, R.J., and Rueda, B.R. (2013). Ovarian cancer stem cells: working towards the root of stemness. *Cancer Lett.* 338, 147–157.
- Fu, D., Holtom, G., Freudiger, C., Zhang, X., and Xie, X.S. (2013). Hyperspectral imaging with stimulated raman scattering by chirped femto-second lasers. *J. Phys. Chem. B* 117, 4634–4640.
- Ginestier, C., Wicinski, J., Cervera, N., Monville, F., Finetti, P., Bertucci, F., Wicha, M.S., Birnbaum, D., and Charafe-Jauffret, E. (2009). Retinoid signaling regulates breast cancer stem cell differentiation. *Cell Cycle* 8, 3297–3302.
- Jia, D., Yang, W., Li, L., Liu, H., Tan, Y., Ooi, S., Chi, L., Filion, L.G., Figeys, D., and Wang, L. (2015). β-Catenin and NF-κB co-activation triggered by TLR3 stimulation facilitates stem cell-like phenotypes in breast cancer. *Cell Death Differ.* 22, 298–310.
- Jordan, C.T., Guzman, M.L., and Noble, M. (2006). Cancer stem cells. *N. Engl. J. Med.* 355, 1253–1261.
- Kamphorst, J.J., Cross, J.R., Fan, J., de Stanchina, E., Mathew, R., White, E.P., Thompson, C.B., and Rabinowitz, J.D. (2013). Hypoxic and Ras-transformed cells support growth by scavenging unsaturated fatty acids from lysophospholipids. *Proc. Natl. Acad. Sci. USA* 110, 8882–8887.
- Karin, M., Cao, Y., Greten, F.R., and Li, Z.W. (2002). NF-κB in cancer: from innocent bystander to major culprit. *Nat. Rev. Cancer* 2, 301–310.
- Lewis, D.A., Travers, J.B., Machado, C., Somani, A.K., and Spandau, D.F. (2011). Reversing the aging stromal phenotype prevents carcinoma initiation. *Aging (Albany, N.Y.)* 3, 407–416.
- Li, S., Kendall, S.E., Raices, R., Finlay, J., Covarrubias, M., Liu, Z., Lowe, G., Lin, Y.H., Teh, Y.H., Leigh, V., et al. (2012). TWIST1 associates with NF-κB subunit RELA via carboxyl-terminal WR domain to promote cell autonomous invasion through IL8 production. *BMC Biol.* 10, <http://dx.doi.org/10.1186/1741-7007-10-73>.
- Liu, G., Lynch, J.K., Freeman, J., Liu, B., Xin, Z., Zhao, H., Serby, M.D., Kym, P.R., Suhar, T.S., Smith, H.T., et al. (2007). Discovery of potent, selective, orally bioavailable stearoyl-CoA desaturase 1 inhibitors. *J. Med. Chem.* 50, 3086–3100.
- Liu, P.P., Liao, J., Tang, Z.J., Wu, W.J., Yang, J., Zeng, Z.L., Hu, Y., Wang, P., Ju, H.Q., Xu, R.H., and Huang, P. (2014). Metabolic regulation of cancer cell side population by glucose through activation of the Akt pathway. *Cell Death Differ.* 21, 124–135.

- Liu, B., Lee, H.J., Zhang, D., Liao, C.-S., Ji, N., Xia, Y., and Cheng, J.-X. (2015). Label-free spectroscopic detection of membrane potential using stimulated Raman scattering. *Appl. Phys. Lett.* **106**, 173704.
- Ma, I., and Allan, A.L. (2011). The role of human aldehyde dehydrogenase in normal and cancer stem cells. *Stem Cell Rev.* **7**, 292–306.
- Ma, X., and Xia, Y. (2014). Pinpointing double bonds in lipids by Paternò-Büchi reactions and mass spectrometry. *Angew. Chem. Int. Ed. Engl.* **53**, 2592–2596.
- Marcato, P., Dean, C.A., Giacomantonio, C.A., and Lee, P.W.K. (2011). Aldehyde dehydrogenase: its role as a cancer stem cell marker comes down to the specific isoform. *Cell Cycle* **10**, 1378–1384.
- Meirelles, K., Benedict, L.A., Dombkowski, D., Pepin, D., Preffer, F.I., Teixeira, J., Tanwar, P.S., Young, R.H., MacLaughlin, D.T., Donahoe, P.K., and Wei, X. (2012). Human ovarian cancer stem/progenitor cells are stimulated by doxorubicin but inhibited by Mullerian inhibiting substance. *Proc. Natl. Acad. Sci. USA* **109**, 2358–2363.
- Miranda-Lorenzo, I., Dorado, J., Lonardo, E., Alcalá, S., Serrano, A.G., Clausell-Tormos, J., Cioffi, M., Megias, D., Zagorac, S., Balic, A., et al. (2014). Intracellular autofluorescence: a biomarker for epithelial cancer stem cells. *Nat. Methods* **11**, 1161–1169.
- Mitra, A.K., Davis, D.A., Tomar, S., Roy, L., Gurler, H., Xie, J., Lantvit, D.D., Cardenas, H., Fang, F., Liu, Y., et al. (2015). In vivo tumor growth of high-grade serous ovarian cancer cell lines. *Gynecol. Oncol.* **138**, 372–377.
- Movasagh, Z., Rehman, S., and Rehman, I.U. (2007). Raman spectroscopy of biological tissues. *Appl. Spectrosc. Rev.* **42**, 493–541.
- Nakamura, M.T., and Nara, T.Y. (2004). Structure, function, and dietary regulation of delta6, delta5, and delta9 desaturases. *Annu. Rev. Nutr.* **24**, 345–376.
- Obukowicz, M.G., Welsch, D.J., Salsgiver, W.J., Martin-Berger, C.L., Chinn, K.S., Duffin, K.L., Raz, A., and Needleman, P. (1998). Novel, selective delta6 or delta5 fatty acid desaturase inhibitors as antiinflammatory agents in mice. *J. Pharmacol. Exp. Ther.* **287**, 157–166.
- Pandey, P.R., Okuda, H., Watabe, M., Pai, S.K., Liu, W., Kobayashi, A., Xing, F., Fukuda, K., Hirota, S., Sugai, T., et al. (2011). Resveratrol suppresses growth of cancer stem-like cells by inhibiting fatty acid synthase. *Breast Cancer Res. Treat.* **130**, 387–398.
- Pattabiraman, D.R., and Weinberg, R.A. (2014). Tackling the cancer stem cells - what challenges do they pose? *Nat. Rev. Drug Discov.* **13**, 497–512.
- Poletto, A.C., Furuya, D.T., David-Silva, A., Ebersbach-Silva, P., Santos, C.L., Corrêa-Giannella, M.L., Passarelli, M., and Machado, U.F. (2015). Oleic and linoleic fatty acids downregulate Slc2a4/GLUT4 expression via NFkB and SREBP1 in skeletal muscle cells. *Mol. Cell. Endocrinol.* **401**, 65–72.
- Ponti, D., Costa, A., Zaffaroni, N., Pratesi, G., Petrangolini, G., Coradini, D., Pilotti, S., Pierotti, M.A., and Daidone, M.G. (2005). Isolation and in vitro propagation of tumorigenic breast cancer cells with stem/progenitor cell properties. *Cancer Res.* **65**, 5506–5511.
- Roongta, U.V., Pabalan, J.G., Wang, X., Ryseck, R.P., Farnolli, J., Henley, B.J., Yang, W.P., Zhu, J., Madireddi, M.T., Lawrence, R.M., et al. (2011). Cancer cell dependence on unsaturated fatty acids implicates stearoyl-CoA desaturase as a target for cancer therapy. *Mol. Cancer Res.* **9**, 1551–1561.
- Sansone, P., Ceccarelli, C., Berishaj, M., Chang, Q., Rajasekhar, V.K., Perna, F., Bowman, R.L., Vidone, M., Daly, L., Nnoli, J., et al. (2016). Self-renewal of CD133(hi) cells by IL6/Notch3 signalling regulates endocrine resistance in metastatic breast cancer. *Nat. Commun.* **7**, 10442, <http://dx.doi.org/10.1038/ncomms10442>.
- Santos, C.R., and Schulze, A. (2012). Lipid metabolism in cancer. *FEBS J.* **279**, 2610–2623.
- Shanmugam, R., Kusumanchi, P., Appaiah, H., Cheng, L., Crooks, P., Neelakantan, S., Peat, T., Klaunig, J., Matthews, W., Nakshatri, H., and Sweeney, C.J. (2011). A water soluble parthenolide analog suppresses in vivo tumor growth of two tobacco-associated cancers, lung and bladder cancer, by targeting NF- $\kappa$ B and generating reactive oxygen species. *Int. J. Cancer* **128**, 2481–2494.
- Shostak, K., and Chariot, A. (2011). NF- $\kappa$ B, stem cells and breast cancer: the links get stronger. *Breast Cancer Res.* **13**, 214–220.
- Silva, I.A., Bai, S., McLean, K., Yang, K., Griffith, K., Thomas, D., Ginestier, C., Johnston, C., Kueck, A., Reynolds, R.K., et al. (2011). Aldehyde dehydrogenase in combination with CD133 defines angiogenic ovarian cancer stem cells that portend poor patient survival. *Cancer Res.* **71**, 3991–4001.
- Slipchenko, M.N., Le, T.T., Chen, H.T., and Cheng, J.-X. (2009). High-speed vibrational imaging and spectral analysis of lipid bodies by compound Raman microscopy. *J. Phys. Chem. B* **113**, 7681–7686.
- Szotek, P.P., Pieretti-Vanmarcke, R., Masiakos, P.T., Dinulescu, D.M., Connolly, D., Foster, R., Dombkowski, D., Preffer, F., MacLaughlin, D.T., and Donahoe, P.K. (2006). Ovarian cancer side population defines cells with stem cell-like characteristics and Mullerian Inhibiting Substance responsiveness. *Proc. Natl. Acad. Sci. USA* **103**, 11154–11159.
- Tirinato, L., Liberale, C., Di Franco, S., Candeloro, P., Benfante, A., La Rocca, R., Potze, L., Marotta, R., Ruffilli, R., Rajamanickam, V.P., et al. (2015). Lipid droplets: a new player in colorectal cancer stem cells unveiled by spectroscopic imaging. *Stem Cells* **33**, 35–44.
- Tumanov, S., Bulusu, V., and Kamphorst, J.J. (2015). Chapter six - analysis of fatty acid metabolism using stable isotope tracers and mass spectrometry. In *Methods Enzymol.*, M.M. Christian, ed. (Academic Press), pp. 197–217.
- van der Zee, M., Sacchetti, A., Cansoy, M., Joosten, R., Teeuwissen, M., Heijmans-Antoniessen, C., Ewing-Graham, P.C., Burger, C.W., Blok, L.J., and Fodde, R. (2015). IL6/JAK1/STAT3 signaling blockade in endometrial cancer affects the ALDHhi/CD126+ stem-like component and reduces tumor burden. *Cancer Res.* **75**, 3608–3622.
- Visvader, J.E., and Lindeman, G.J. (2008). Cancer stem cells in solid tumours: accumulating evidence and unresolved questions. *Nat. Rev. Cancer* **8**, 755–768.
- Wang, H.-W., Bao, N., Le, T.L., Lu, C., and Cheng, J.-X. (2008). Microfluidic CARS cytometry. *Opt. Express* **16**, 5782–5789.
- Wang, X., Sun, Y., Wong, J., and Conklin, D.S. (2013). PPAR $\gamma$  maintains ERBB2-positive breast cancer stem cells. *Oncogene* **32**, 5512–5521.
- Yang, W.C., Adamec, J., and Regnier, F.E. (2007). Enhancement of the LC/MS analysis of fatty acids through derivatization and stable isotope coding. *Anal. Chem.* **79**, 5150–5157.
- Zhang, C., Zhang, D., and Cheng, J.-X. (2015). Coherent Raman scattering microscopy in biology and medicine. *Annu. Rev. Biomed. Eng.* **17**, 415–445.
- Zhou, J., and Zhang, Y. (2008). Cancer stem cells: models, mechanisms and implications for improved treatment. *Cell Cycle* **7**, 1360–1370.
- Zhou, B.B., Zhang, H., Damelin, M., Geles, K.G., Grindley, J.C., and Dirks, P.B. (2009). Tumour-initiating cells: challenges and opportunities for anticancer drug discovery. *Nat. Rev. Drug Discov.* **8**, 806–823.

**STAR★METHODS****KEY RESOURCES TABLE**

REAGENT or RESOURCE	SOURCE	IDENTIFIER
<b>Antibodies</b>		
NF-κB p65 (D14E12) XP® Rabbit mAb	Cell Signaling Technology	Cat # 8242S; RRID: AB_10859369
Allophycocyanin (APC) conjugated CD133/1 (AC133) antibody	Miltenyi Biotec	Cat # 130-098-829; RRID: AB_244340
Normal Rabbit control IgG	Santa Cruz Biotechnology	Cat # sc-2027; RRID:AB_737197
APC Mouse IgG2a, κ Isotype Control; Clone #G155-178	BD Biosciences	Cat # 555576; RRID:AB_398604
<b>Chemicals, Peptides, and Recombinant Proteins</b>		
CAY 10566	Santa Cruz Biotechnology	Cat # sc-205109
SC26196	Santa Cruz Biotechnology	Cat # sc-361350
D-Glucose (U-13C6, 99%)	Cambridge Isotope Laboratories	Cat # CLM-1396
L-Glutamine (U-13C5, 99%)	Cambridge Isotope Laboratories	Cat # CLM-1822
MammoCult Human medium kit	StemCell Technologies	Cat # 05620
DMEM high glucose medium	Corning	Cat # 10-017-CV
Fatty acids (including 16:0, 16:1, 18:0, 18:1, 18:2, 20:4, 22:6)	Sigma	Cat #P0500, #P9417, #4751, #O1008, #L1376, #10931, #D2534
DMAPT (NF-κB inhibitor)	Abcam	Cat # ab146189
DMSO	Sigma-Aldrich	Cat # D2650
CM037 (ALDH inhibitor)	Chemical Genomics Core Facility (IU, Indianapolis, IN)	Dr. Zhong-Yin Zhang (Purdue University, West Lafayette, IN)
Retinoic acid	Sigma-Aldrich	Cat # R2625
DreamFect Gold Transfection Reagent	OZ Biosciences	DG81000
iTaq Universal SYBR® Green Supermix	Bio-Rad	Cat # 1725120
RNA STAT-60	Tel-Test Inc.	Cat # Cs-502
<b>Critical Commercial Assays</b>		
Cell Counting Kit-8 (CCK-8) assay	Dojindo Molecular Technologies	Cat # CK04-05
ALDEFLUOR assay kit	StemCell Technologies	Cat # 01700
Dual-Luciferase Reporter Assay	Promega	Cat # E1910
iScript cDNA Synthesis Kit	Bio-Rad	Cat # 1708890
Human Cancer Stem Cell RT <sup>2</sup> Profiler PCR Array	QIAGEN	Cat # PAHS-176ZC
QIAquick PCR Purification Kit	QIAGEN	Cat# 28104
Chromatin Immunoprecipitation (ChIP) Assay Kit	Millipore	Cat # 17-295
<b>Experimental Models: Cell Lines</b>		
Human ovarian cancer COV362 cells	Mitra et al., 2015	Dr. Kenneth P. Nepheu (IU, Bloomington, IN)
Human ovarian cancer OVCAR5 cells	Mitra et al., 2015	Dr. Kenneth P. Nepheu (IU, Bloomington, IN)
Normal human dermal fibroblasts NHF544	Lewis et al., 2011	Dr. Dan Spandau (IUSCC, Indianapolis, IN)
Primary ovarian carcinoma cells	This paper	See Table S1 for details
<b>Experimental Models: Organisms/Strains</b>		
Athymic nude mice; strain: Hsd:Athymic Nude-Foxn1 <sup>nu</sup>	Envigo	N/A
<b>Recombinant DNA</b>		
pQCXIP-p65	Chua et al., 2007	Dr. Harikrishna Nakshatri (IUSM, Indianapolis, IN)
SCD shRNA (h) Lentiviral Particles	Santa Cruz Biotechnology	Cat # sc-36464-V

(Continued on next page)

**Continued**

REAGENT or RESOURCE	SOURCE	IDENTIFIER
Control shRNA Lentiviral Particles-A	Santa Cruz Biotechnology	Cat # sc-108080
Sequence-Based Reagents		
See <a href="#">Table S3</a> for primers used for RT-PCR and ChIP assay	This paper	N/A
Software and Algorithms		
ImageJ	NIH public software	N/A
Agilent MassHunter Workstation Software Quantitative Analysis	Agilent Technologies	N/A
Other		
See <a href="#">STAR Methods</a> for resources used for hyperspectral SRS imaging, Raman spectroscopy, and Mass spectrometry	This paper	N/A

**CONTACT FOR REAGENT AND RESOURCE SHARING**

Further information and requests may be directed to, and will be fulfilled by, the Lead Contact, Ji-Xin Cheng ([jcheng@purdue.edu](mailto:jcheng@purdue.edu)).

**EXPERIMENTAL MODEL AND SUBJECT DETAILS****Cell lines**

Human ovarian cancer cell lines COV362 and OVCAR5 were a gift from Dr. Kenneth P. Nephew (Indiana University, Bloomington, IN). Both cell lines were tested to be mycoplasma negative and authenticated by Short Tandem Repeat (STR) analysis. COV362 cells were cultured in DMEM high glucose medium supplemented with 10% FBS and 100 units/mL penicillin and 100 µg/mL streptomycin. OVCAR5 cells were grown in D-MEM (high glucose), 10% fetal bovine serum (FBS), 0.1 mM Non-Essential Amino Acids (NEAA), 2 mM L-glutamine, and antibiotics. All cells were cultured at 37°C in a humidified incubator with 5% CO<sub>2</sub> supply.

**Primary human cells**

De-identified malignant ascites fluid specimens from ovarian cancer patients (n = 4) were obtained at the Indiana University Simon Cancer Center (IUSCC) under an IRB approved protocol (IUCRO#505). Additional information regarding subjects' clinical history is provided in [Table S1](#). The normal human dermal fibroblasts were obtained and provided by Dr. Dan Spandau (IUSCC, Indianapolis, IN) after isolation from foreskin tissue. The procedures related to human tissue samples procurement were approved by the Indiana University School of Medicine IRB.

Tumor cells were purified as previously described ([Condello et al., 2015](#)). After centrifugation at 1,200 rpm for 5 min, 25,000 ascites derived tumor cells were cultured as monolayers in DMEM medium supplemented with 10% FBS and antibiotics or suspended in Mammocult Complete medium (StemCell Technologies) and plated in ultra-low adherent surfaces to allow spheroid formation.

**Subcutaneous xenograft mouse model**

All animal experiments were conducted following protocols approved by Purdue Animal Care and Use Committee (PACUC). 5~6 week-old female athymic nude mice (strain Hsd:Athymic Nude-Foxn1<sup>nu</sup>) (Envigo) were used to establish the tumor subcutaneous xenograft model. Housing and husbandry of the nude mice were conducted by the staffs at the animal facility of Purdue University following PACUC regulations.

**METHOD DETAILS****Sphere formation assay**

FACS-sorted ALDH<sup>+</sup>/CD133<sup>+</sup> OC cell lines or primary cells were seeded as single cell suspension at a concentration of 10,000 cells/well in 96-well ultra-low attachment plates (Corning, Corning, NY, USA) in Mammocult complete medium (StemCell Technologies). After 6 days, spheroids were counted after centrifugation at 300xg for 5 min. Cell numbers were also quantified by the CCK-8 assay (Dojindo Molecular Technologies, Rockville, MD). All assays were performed in four replicates.

**Aldefluor assay and Fluorescence-Activated Cell Sorting**

ALDH and CD133 double positive or negative cells were isolated by fluorescence-activated cell sorting (FACS) using the Aldefluor assay kit (StemCell Technologies, Inc.) and the allophycocyanin (APC) conjugated CD133/1 (AC133) antibody (Miltenyi Biotec, Auburn, CA, USA). Briefly, dissociated monolayer single cells were resuspended in Aldefluor assay buffer containing the ALDH1 substrate, bodipyaminoacetaldehyde (BAAA), at 1.5mM. After incubation for 45 min at 37°C, the cells were centrifuged at 1,200 rpm for 5 min at 4°C, washed twice with Aldefluor assay buffer and incubated in the same buffer supplemented with 0.5% bovine serum albumin BSA and anti-CD133/1 (AC133) antibody (1:10 dilution) for 30 min on ice. The test ALDH<sup>+</sup>/CD133<sup>+</sup> population was gated

using control cells incubated under an identical condition in the presence of a 10-fold molar excess of the ALDH inhibitor (DEAB), and anti-mouse IgG1 isotype control APC-conjugated antibody (1:10 dilution) (Miltenyi Biotec). FACS was performed using a FACS Aria II flow cytometer (BD Biosciences, San Jose, CA) under sterile conditions.

### Hyperspectral stimulated Raman scattering (SRS) imaging

Hyperspectral SRS imaging was done with a spectral focusing method following previously published protocol (Fu et al., 2013; Liu et al., 2015). Briefly, the Raman shift is tuned by controlled the temporal delay between two chirped femtosecond pulses. In our scheme, a femtosecond laser (Coherent) operating at 80 MHz provided the pump and Stokes laser source. With pump beam tuned to 810 nm, Stokes beam was tuned to 1055 nm to cover the C-H vibration region. The Stokes beam was modulated at 2.3 MHz by an acousto-optic modulator (1205-C, Isomet). After combination, both beams were chirped by two 12.7 cm long SF57 glass rods and then sent to a laser-scanning microscope. A 60x water immersion objective (NA = 1.2, UPlanApo/IR, Olympus) was used to focus the light on the sample, and an oil condenser (NA = 1.4, U-AAC, Olympus) was used to collect the signal.

To obtain a hyperspectral SRS image, a stack of 50 images at different pump-Stokes temporal delay was recorded. The temporal delay was controlled by an automatic stage, which moved forward with a step size of 10  $\mu\text{m}$ , corresponding to  $\sim 5 \text{ cm}^{-1}$ . To calibrate the Raman shift to the temporal delay, standard chemicals with known Raman peaks in C-H region from 2800 to 3050  $\text{cm}^{-1}$ , including DMSO, methanol, oleic acid, and linolenic acid, were used. To eliminate the power difference at different Raman shift, SRS signal was normalized by two-photon absorption signal from Rhodamine 6G, the cross-section of which is considered constant in this small region. The spectral resolution of the system was estimated to be  $\sim 25 \text{ cm}^{-1}$ . Hyperspectral SRS images were analyzed using software ImageJ.

### Spontaneous Raman spectroscopy

Confocal Raman spectral analysis from individual LDs was performed as described previously (Slipchenko et al., 2009). A 5-pico-second laser at 707 nm was used as excitation beam for Raman spectral acquisition. Acquisition time for a typical spectrum from individual LDs was 20 s, with the beam power maintained around 15 mW at the sample. For each specimen, at least 10 spectra from individual LDs in different locations or cells were obtained. The spectra were analyzed using software Origin 8.5. The background was removed manually, and peak height was measured.

### Mass spectrometry analysis of fatty acids

OVCAR5, COV362 and primary human OC cells were cultured under serum-free conditions either as monolayers or spheres. For the  $^{13}\text{C}$  tracing experiments, cells were seeded in ultra-low adherence plates and grown in sphere culture medium (containing glucose and glutamine) supplemented with additional 25 mM Glucose ( $\text{U-}^{13}\text{C}_6$ , 99%) and 4 mM L-Glutamine ( $\text{U-}^{13}\text{C}_5$ , 99%). The cells were grown as spheres for 6 days with or without inhibitor treatment or SCD1 shRNA knockdown. Spheres were collected by centrifuging at 200 rpm for 1 min to separate from floating single cells. All the experiments were conducted in three replicated sets of samples.

Free fatty acid extraction was performed following previous protocol (Ma and Xia, 2014). Cell pellets were resuspended in 300  $\mu\text{L}$  PBS, mixed with 1 mL methanol and acidified with HCl to 25 mM final concentration. After addition of 1 mL isoctane was added, and samples were vortexed and centrifuged at 3,000 g for 1 min. The top layer was transferred to a glass tube and dried under vacuum. Extracted lipids were re-dissolved in 100  $\mu\text{l}$  acetone: water (1:1). Electrospray Ionization-Mass Spectrometry (ESI-MS) analysis of fatty acids was conducted.

Extraction and preparation of saponified fatty acids were performed following previous protocol (Kamphorst et al., 2013; Yang et al., 2007). Briefly, cells were lysed in 1 mL of cold 50:50 MeOH/H<sub>2</sub>O solution with 0.1 M HCl, mixed with 0.5 mL chloroform, and centrifuged at 16,000 g for 5 min. The lower phase was transferred to glass vials and dried under N<sub>2</sub> flow. Dried lipid extract was reconstituted into 90:10 MeOH/H<sub>2</sub>O containing 0.3 M KOH, saponified at 80°C for 1 hr, and then acidified with 0.1 mL of formic acid. Fatty acids were extracted twice with 1 mL of hexane, dried under N<sub>2</sub> flow. For quantitative analysis, each fatty acid (Sigma) at known concentration were used as internal standards. Liquid Chromatography-Mass Spectrometry (LC-MS) analysis of fatty acids was performed following previously described protocol (Yang et al., 2007). For  $^{13}\text{C}$  tracing experiments, fatty acids (e.g., FA 16:0, 16:1, 18:0, 18:1) with various numbers of  $^{13}\text{C}$  labeling were analyzed. The natural isotopic abundances were correlated following described protocol (Tumanov et al., 2015).

### Tumor initiation assays in subcutaneous xenograft mouse model

For tumor formation and growth experiment, FACS-isolated ALDH<sup>+</sup>/CD133<sup>+</sup> OVCAR5 cells were seeded at a density of 20,000 cells/well in non-adherent ultra-low plates in Mammocult complete medium (StemCell Technologies), and treated with DMSO, CAY10566 or SC26196 respectively at a concentration of 1  $\mu\text{M}$  for 6 days. Spheres were collected and mixed with equal volume of Matrigel Matrix (Corning, Cat# 356234) prior to subcutaneous injection. An equal number of DMSO and inhibitors treated spheres were injected subcutaneously into the left and right flank of 5~6 week-old female athymic nude mice (Envigo), respectively, with 8 mice randomly assigned to each group. Tumors were measured twice a week using calipers. Tumor volume was calculated as  $1/2 \times L \times W^2$ , where L stands for the length, and W for the width measured by a caliper in mm. Time to tumor formation was defined as the time from cell inoculation to the time when tumors were first detected. At the end of the study (e.g., when at least one tumor reached 2,000 mm<sup>3</sup>), mice were euthanized, tumors were harvested, measured and weighed.

For tumor initiation assay, FACS-isolated ALDH<sup>+</sup>/CD133<sup>+</sup> OVCAR5 cells were seeded in non-adherent ultra-low 96-well plates at densities of 20,000, 10,000, 5,000, 1,000, and 500 cells per well. The cells were treated with DMSO or CAY10566 at a concentration of 1 μM and grown as spheroids for 6 days. Tumor cell inoculation was performed as described above with 5 mice randomly assigned to each group. Tumor initiation was determined ~30 days after tumor cell inoculation.

#### **Generation of SCD1 stably knockdown cells**

OVCAR5 and COV362 cells were transfected with SCD1 targeting shRNA lentiviral particles (Santa Cruz Biotechnology, Inc., Dallas, TX, sc-36464-V) following the manufacturer's protocol. Scrambled shRNA lentiviral particles (Santa Cruz, sc-108080) were used as a control. Stably transfected cells were selected with 0.5 μg/ml puromycin.

#### **Stable retroviral transduction**

The active p65 (Rel A) subunit of NF-κB subcloned into the pQCXIP retroviral vector (Chua et al., 2007) was transduced in OVCAR5 and COV362 cells and pooled colonies were selected with puromycin. Transduction of the empty vector was performed in parallel.

#### **Gene reporter assay**

Dual-Luciferase Assay (Promega, Madison, WI) quantified NF-κB activity in COV362, OVCAR5 and primary cells grown as spheroids, according to the manufacturer's instructions. In brief, cells were plated in ultra-low adherence plates in Mammocult complete medium and transiently co-transfected with the NF-κB promoter luciferase and renilla plasmids at the ratio of 10:1 by using DreamFect Gold transfection reagent (OZ Biosciences, Marseille, France). After 24 hr, cells were treated with the SCD1 inhibitor CAY10566 or the Δ6 inhibitor SC26196 at a concentration of 1.0 μM for 48 hr. Luminescence was measured by using the TD-20/20 Luminometer (Turner Biosystems, Madison, WI). Experiments were performed in triplicate and repeated two times in independent conditions. To control for transfection efficiency, NF-κB luminescence was normalized to renilla activity.

#### **Reverse transcription-PCR (RT-PCR)**

Total RNA was extracted from OC cell lines or primary cells by using RNA STAT-60 (Tel-Test Inc., Friendswood, TX) and reverse transcribed using iScript cDNA Synthesis Kit (Bio-Rad, Hercules, CA). The reverse transcriptase product (1 μL) and primers (Table S3) were heated at 94°C for 10 min, followed by 40 cycles of amplification at 94°C for 15 s and 60°C for 1 min. At the end of the PCR reaction a melting curve was generated and the cycle threshold (Ct) was recorded for the reference and control genes. The relative expression of different transcripts was calculated as ΔCt and normalized by subtracting the Ct of target genes from that of the house-keeping control (18S). Real-time PCR was carried out on an ABI Prism 7900 platform (Applied Biosystems, Grand Island, NY) using the iTaq universal SYBR Green super mix (Bio-Rad, Hercules, CA, USA). Human IL6 gene expression was detected using TaqMan® Gene Expression Assay (Hs00985639\_m1) and TaqMan® Gene Expression Master Mix (Applied Biosystems). Results are presented as means + SEM of replicates. Measurements were performed in duplicate and experiments were run three times in independent conditions.

The human cancer stem cells RT<sup>2</sup> Profiler PCR Array was purchased from SA Bioscience and real-time PCR was performed on ABI Prism 7900 HT (Applied Biosystems), according to the manufacturer's instructions. Data analysis was performed based on the ΔΔCt method with normalization of the raw data to the housekeeping genes using a Microsoft excel algorithm provided by the manufacturer. An ontology classification assignment for each gene was performed, and fold-changes were calculated and expressed as percent of composition for each represented pathway in control versus treated spheres.

#### **Chromatin immunoprecipitation (ChIP)**

Chromatin immunoprecipitation was performed by using a kit from EMD Millipore (Billerica, MA USA) according to the manufacturer's instructions, with some modifications. In brief, 10<sup>7</sup> OVCAR5 cells stably transduced with pQCXIP and pQCXIP/p65 were fixed in 1% formaldehyde for 10 min at 37°C to cross-link histones to DNA. Cells were washed twice with ice-cold phosphate-buffered saline (10 mmol/L Na2HPO4, 2 mmol/L NaH2PO4, 137 mmol/L NaCl, 2.7 mmol/L KCl) containing protease inhibitors (1 μg/mL aprotinin, 1 μg/mL leupeptin, and 1 mmol/L phenylmethylsulfonyl fluoride) and lysed for 10 min in SDS buffer (1% SDS, 50 mM Tris [pH 8.1], 10 mM EDTA). Cell lysates were sonicated on ice with 3 sets of 10 s pulses using a Sonic Dismembrator Model 100 (Fisher Scientific, Pittsburgh, PA) set at 30% of maximum power. The soluble chromatin was then centrifuged, resuspended in ChIP dilution buffer (final concentration of 15 mmol/L Tris-HCl [pH 8.1], 2 mmol/L EDTA, 150 mmol/L NaCl, 0.1% SDS, 1% Triton X-100) containing protease inhibitors, and one tenth of the supernatant was used as DNA input control. The remaining volume of ChIP solution was pre-cleared by incubation with sheared salmon sperm DNA/protein A-agarose 50% slurry and incubated with rabbit immunoglobulin G (IgG) or rabbit polyclonal anti-NF-κB p65 antibody (Cell Signaling Technology Inc., 1:100 dilution) overnight at 4°C with agitation. The immunoprecipitated complexes were incubated with protein A slurry and then washed successively with low-salt buffer (0.1% SDS, 1% Triton X-100, 2 mM EDTA, 20 mM Tris-HCl [pH 8.1], 150 mM NaCl), high-salt buffer (500 mM NaCl), LiCl buffer (0.25 M LiCl, 1% IGEPAL-CA630, 1% deoxycholate, 1 mM EDTA, 10 mM Tris-HCl [pH 8.1]), and Tris-EDTA (pH 8.0), and then were eluted with 1% SDS, 100 mM NaHCO<sub>3</sub> buffer. The cross-linking of protein-DNA complexes was reversed by incubation with 5 M NaCl at 65°C for 4 hr, and DNA was digested with 10 mg of proteinase K (Sigma)/ml for 1 hr at 45°C before DNA extraction.

To detect whether NF-κB p65 binds to the SCD1 promoter, input and immunoprecipitated chromatin was extracted with QIAquick PCR purification kit (QIAGEN, Valencia, CA) by following the manufacturer's protocol and subjected to PCR amplification using

primers designed for the putative p65 binding region 1 (SCD F1/R1) and putative p65 binding region 2 (SCD F2/R2) in the *SCD1* promoter ([Table S3](#)). The PCR products were analyzed by real-time PCR and normalized by subtracting the Ct of target genes from that of the input/starting material. The expression levels of target genes were calculated as fold changes compared to the signal of DNA immunoprecipitated with IgG (control). As a positive control, DNA immunoprecipitated with p65 antibody was amplified using primers for the known sequence of the *IL8* promoter ([Table S3](#)) ([Li et al., 2012](#)), known NF- $\kappa$ B target gene. As a negative control, DNA immunoprecipitated with p65 antibody was amplified with primers designed for the *SCD1* promoter, upstream of the putative p65 binding sites (SCD upstream). All the measurements were performed in triplicates.

#### QUANTIFICATION AND STATISTICAL ANALYSIS

Hyperspectral SRS images were quantitatively analyzed using ImageJ software. Raman spectroscopy data were analyzed using Origin 8.5 software. Mass spectrometry data were analyzed using Agilent MassHunter Workstation Software Quantitative Analysis. One-way ANOVA or Student's t test were used for comparisons between groups. Results are represented as means  $+$   $\pm$  SEM or as indicated. Each experiment was performed with a minimum of three biological replicates; exact numbers are indicated in associated figure legends. Significant differences were considered at \*  $p < 0.05$ , \*\*  $p < 0.01$ , and \*\*\*  $p < 0.001$ . n.s. means not significant.